

Temporal and spatial intermittencies within channel flow turbulence near transition

Anubhav Kushwaha, Jae Sung Park, and Michael D. Graham*

*Department of Chemical and Biological Engineering, University of Wisconsin-Madison,
Madison, Wisconsin 53706-1691, USA*

(Received 26 April 2016; published 24 February 2017)

Direct numerical simulations (DNS) of plane Poiseuille flow are performed in an extended domain at friction Reynolds numbers ranging from 70 to 100. In minimal domains, turbulence in this Reynolds number range displays substantial intermittency that is associated with chaotic movement of turbulent trajectories between lower and upper branch invariant solutions known as exact coherent states (ECS). The present work aims to address the relationship between temporal dynamics in minimal channels and spatiotemporal dynamics in extended domains. Both temporal and spatial analyses of the turbulent velocity fields are performed, the latter using image analysis methods. These analyses partition the flow characteristics into low-, intermediate- and high-drag classes; we present the differences between flows fields in these classes in terms of simple quantities like mean velocity, wall shear stress, and flow structures. The temporal and spatial analysis methods, although completely independent of one another, yield very similar results for both low- and high-drag regions. In particular, the conditional mean profiles in regions of low drag closely resemble those found in low-drag temporal intervals in the minimal channel. Finally, we address the possibility of similarities between turbulence and exact coherent states in two ways: (1) comparing wall shear stress in localized patches the size of minimal channels in large domains with those in actual minimal channel and (2) comparing conditional mean velocity profiles during low-drag events with mean profiles from lower branch ECS. These analyses show that both the local near-wall flow structure in the low-drag patches of the large domain and the conditional mean profiles in the region $y^+ \lesssim 30$ resemble those of a lower branch minimal domain ECS. In summary, the results presented here suggest that spatiotemporal intermittency in transitional channel flow turbulence is related to temporal intermittency, and by extension to the state space structure, in the minimal channel.

DOI: [10.1103/PhysRevFluids.2.024603](https://doi.org/10.1103/PhysRevFluids.2.024603)

I. INTRODUCTION

The past 20 years or so have seen rapid advances in understanding transition to turbulence [1–5]. These advances build on the mathematical foundation of dynamical systems theory and the discovery of nontrivial invariant solutions to the Navier-Stokes equations (NSE) for the canonical shear flows: plane Couette flow [6–17], plane Poiseuille flow [18–22], and pipe flow [2,3,23–27]. These solutions, sometimes called exact coherent states (ECS) [18], take the form of steady states, nonlinear traveling waves, relative periodic orbits, and edge states (these are solutions that live on the boundary in state space of the basins of attraction of the laminar and turbulent states, respectively). Most of these states have been found in so-called minimal flow units (MFU) or minimal channel geometries, i.e., they are spatially periodic in the unbounded dimensions of the domain with periods that roughly correspond to the smallest length scales at which turbulence can persist in the domain of interest. The spatial structure of these solutions qualitatively matches that of near-wall turbulence: a mean shear flow with streamwise-modulated streamwise vortices that generate low- and high-speed streaks. Additionally,

*Corresponding author: mdgraham@wisc.edu

direct numerical simulations of turbulence in MFUs indicates that at low (transitional) Reynolds numbers, the turbulent trajectories in these geometries are organized at least in part around the ECS [5,10,28]. It is important to note that some highly localized invariant solutions, which display nontrivial flow only over a small region of an extended flow domain, while the remainder of the domain remains laminar, have been found as well [29–31]. These solutions are highly reminiscent of the turbulent spots or puffs that are a common feature of turbulence near transition [32].

More broadly, the spatiotemporal dynamics of turbulence in extended domains contains many open issues even in the transitional Reynolds number regime. One of these is the extent to which dynamics in extended domains is related to dynamics in minimal ones. Aiming to shed some light on these issues, the present work focuses on the plane channel flow geometry, using direct numerical simulations and temporal and spatial sampling techniques to characterize intervals and regions of high and low turbulence activity. Specifically, our results are consistent with the hypothesis that temporal intermittency observed in minimal channels becomes spatiotemporal in extended domains and that main features of the ECS and minimal channel turbulence results are found in localized regions in the extended domain.

A number of research groups have computed exact coherent states for the channel flow geometry [19,20,22,28,33,34]. For the most part, these solutions arise in pairs at saddle-node bifurcations; the upper branch (UB) solution of each pair has larger velocity fluctuations and higher drag compared to the lower branch (LB) solution. Park and Graham [28] found a family of channel flow ECS in the minimal channel geometry, which they denoted “P4”, that has particularly intriguing behavior. The mean velocity profile of the upper branch state approaches the Prandtl–von Kármán log-law while that of the lower branch approaches a form generally associated with turbulence in viscoelastic polymer solutions, the so-called Virk profile [35]. This profile is a good approximation of experimental and computational observations in the so-called maximum drag reduction (MDR) regime. This ECS result adds to the set of observations in which mean velocity profiles close to the Virk profile are found in Newtonian flow [36–42]. Notwithstanding this intriguing similarity to MDR, the present work addresses only Newtonian flow. The flow structures of the upper and lower branch solutions are very different—the upper branch has strong streamwise vortices and wavy streaks representing strong fluctuations while the lower branch has weak vortices and almost streamwise-invariant streaks.

Direct numerical simulations (DNS) of turbulence in the same minimal geometry at Reynolds numbers near transition have been found by a number of researchers [39,42,43] to exhibit temporal intermittency between high- and low-drag intervals: Xi and Graham [39] denoted these as active and hibernating, respectively. Park and Graham [28] found that this behavior is a reflection of the organization of the turbulent dynamics around the P4 solution family. Specifically, as illustrated in Fig. 1(a), at friction Reynolds number $Re_\tau = 85$ the trajectory spends most of its time orbiting in the vicinity of the upper branch solution, displaying relatively high drag and a mean profile near the von Kármán profile, but occasionally takes excursions that approach the lower branch solutions (there are actually two of these because the lower branch turns back on itself) and thus exhibit low drag. Over part of the Reynolds number regime the lower branch states lie on the basin boundary between the laminar and turbulent attractors in the minimal domain, so the approach of the turbulent dynamics to these states implies an approach to the laminar-turbulent basin boundary. At higher Reynolds number, these excursions become increasingly rare, as we describe below. Mean velocity profiles of some upper and lower branch traveling wave solutions from the P4 family are plotted in Fig. 1(b). As noted above, the upper branch velocity profiles nearly collapse with the classical Newtonian (von Kármán) profile, while the lower branch velocity profiles approach the Virk MDR. Park and Graham [28] showed that near the wall ($y^+ \lesssim 30$), instantaneous velocity profiles from minimal channel DNS are very nearly bracketed between the UB and LB solutions, while deviations from these solutions are observed near the center of the channel. Thus, the P4 traveling waves appear to form an approximate envelope for the DNS mean velocity profiles for $y^+ \lesssim 30$. This is important as these similarities in the near-wall behavior suggest that the turbulent dynamics in minimal channels is organized at least in part around these traveling wave solutions.

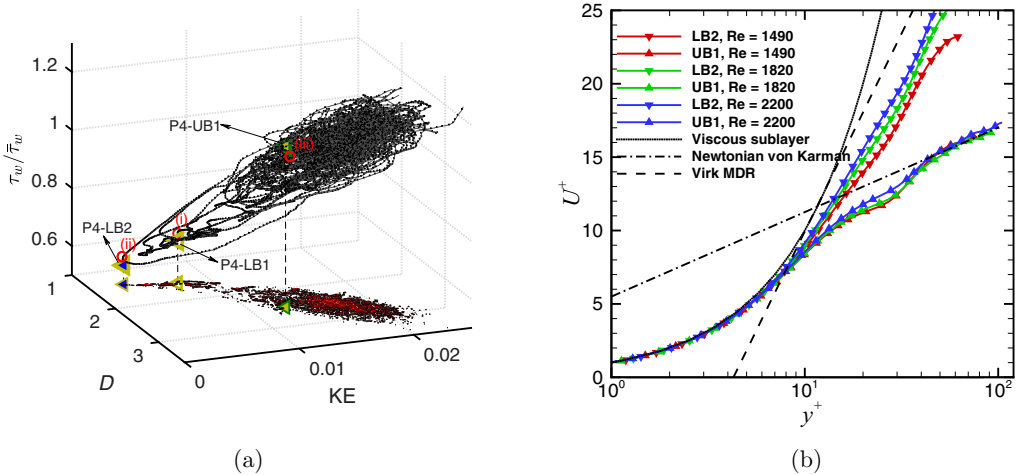


FIG. 1. (a) State-space visualization of DNS trajectories in a minimal channel turbulent flow [$L_x \times L_y \times L_z = \pi \times 2 \times \pi/2$, $Re_c = 1800$ ($Re_\tau = 85$), constant mass flux], projected onto three dimensions: disturbance kinetic energy (KE), energy dissipation rate (D), and normalized instantaneous wall shear stress ($\tau_w/\bar{\tau}_w$) [28]. The gray line indicates the turbulent trajectory, to which black dots are attached at intervals of $11/U_c$. The joint probability density of KE and D is shown at the bottom of the figure. The labeled symbols (<) are P4 solutions. Points (i), (ii), and (iii) are the closest approaches to P4-LB1, P4-LB2, and P4-UB1, respectively. All quantities are calculated only for the bottom half of the channel. (b) Mean velocity profiles of lower (LB) and upper branch (UB) traveling waves of the P4 family. These solutions are also being used for comparison with DNS (Sec. III B 2).

A natural question is how closely these minimal channel observations are related to the phenomenon of laminar-turbulent intermittency in the transitional Reynolds number regime for spatially extended flows (i.e., experimentally realized flows where no artificial periodicities are present). Manneville [44] provides an excellent overview of this phenomenon; the basic observation is that the transitional Reynolds number regime, at a given point in the domain the flow alternates randomly between states with weak and strong fluctuations. Pipe flow is the most well-studied case. Here laminar-turbulent intermittency is first observed as localized turbulent patches, known as puffs, surrounded by laminar flow upstream and downstream of it [45,46]. These puffs have complex behavior, involving growth and splitting [3,47], and many aspects of the transition regime can be captured using reaction-diffusion-advection models involving evolving fronts that separate spatial regions of turbulent and laminar motions [48–50], with the turbulent regions taking over the whole domain once the Reynolds number is sufficiently high. Nevertheless, even at Reynolds numbers traditionally regarded as above the transition regime, substantial spatiotemporal fluctuations in turbulence activity persist [51]. In the case of boundary layer flows, turbulent spots are surrounded by laminar flow [52]. These spots spread in all directions as they convect downstream [53,54], culminating in a fully turbulent boundary layer. In channel flow, the focus of the present work, experimental studies by Carlson *et al.* [55] reveal the presence of arrowhead-shaped turbulent spots with streamwise streaks trailing from the rear of the spot. The front of the spot moves faster than the rear end, resulting in the expansion of the spot before it eventually splits into two. Within a spot, strong turbulent fluctuations occur, which are preceded by oblique waves that surround the spot. Other studies [56–63] observed elongated near-wall streaks forming stripe patterns. These patterns are oriented obliquely relative to the main flow direction. Flow is highly turbulent near the center region of the stripes, and around the stripes are regions of streamwise streaks that are relatively less turbulent. As the Reynolds number is increased, the fluctuation intensity in the less turbulent regions increases along both streamwise and spanwise directions, the stripiness in the flow structures start to

vanish, and eventually the flow becomes uniformly turbulent, i.e., any apparent large-scale structures are absent.

To differentiate between regions of turbulent flow from nonturbulent flow, conditional sampling techniques have been used by many researchers. Volino *et al.* [64] conducted transitional boundary layer experiments in a wind tunnel and measured velocities at several locations in the streamwise and wall-normal directions. They calculated intermittency factors using flow quantities such as streamwise velocity and Reynolds shear stress, and found that the mean velocity profiles differed significantly between the turbulent and nonturbulent regimes. They also showed that the wall-normal velocity fluctuations and Reynolds shear stress in the turbulent spots are significantly higher and the skin friction was 70% higher within the turbulent zone compared to the nonturbulent zone. However, no data on the flow structures in the turbulent and nonturbulent zones were reported. Hutchins *et al.* [65] identified conditional structures during low- or high-skin-friction events in a turbulent boundary layer flow. They defined a low-skin-friction event as an event during which the instantaneous skin-friction fluctuation is negative, and vice versa, and found that the mean velocity profile during low-skin-friction events lie well above the velocity profiles during high-skin-friction events, which is same as the findings of Volino *et al.* [64]. In addition, the conditional flow fields reveal the presence of an elongated low-speed structure aligned in the flow direction flanked on either side by a pair of counter-rotating vortices [66,67].

A conceptually simple technique of conditionally partitioning data sets such as flow fields into distinct groups or *clusters* such that properties in the same cluster are more similar to each other than those in other clusters is *k*-means clustering. Kaiser *et al.* [68] used this method to partition snapshots from a mixing layer flow into *k* distinct clusters. The mean or *centroid* of each cluster is determined iteratively by minimizing the sum of squares of distances between individual snapshots of a cluster and the centroid of that cluster. This results in the formation of *k* different clusters such that properties are similar within a cluster but vary from one cluster to the other. Another approach to partitioning large data sets is *thresholding*. Nolan and Zaki [54] performed numerical studies for boundary layer flows and developed a thresholding technique to discriminate laminar spots from turbulent spots. An input signal, which is a time series of flow properties, e.g., velocity fluctuations, is carefully thresholded using Otsu's method [69]—an image-processing technique used to automatically perform image segmentation by determining threshold(s) between distinct regions such that each region shares certain characteristics. Otsu's method picks out the optimum threshold(s) by minimizing the *intra*class variance, or maximizing the *inter*class variance. It can also be used for multilevel thresholding; in general, the number of classes is one more than the number of thresholds. Although the *k*-means and Otsu algorithms are different, it can be shown that they both extremize the same objective function [70]. Nolan and Zaki identified laminar and turbulent regions in boundary layer flows and computed conditional averages for those distinct regions. They observed that the laminar-conditioned velocity profiles have a characteristic laminar shape whereas the turbulent-conditioned profiles follow the law of the wall. We use Otsu's method below.

Many other methods for discriminating turbulent areas from nonturbulent regions in a flow field have been employed where thresholds are set for various flow properties. For example, instantaneous wall-normal and spanwise velocities, instantaneous turbulent dissipation and vortex identification (λ_2 and Q criteria) are thresholded by Rehill *et al.* [71] in a boundary layer flow over a flat plate. They found that the Q criterion and the dissipation methods show the least sensitivity to changes in the threshold level and hence are the best input signals that can be used for identifying turbulent spots. Baltzer *et al.* [72] examined and characterized the spatial arrangements of very large-scale motions in a pipe flow at high Reynolds number. Regions at a distance of $y/R = 0.15$ from the pipe wall where the streamwise velocity fluctuations were stronger than the threshold value u'_{thr} of $-0.10U_{\text{bulk}}$ were extracted—these are the low-speed regions in the flow field. A conditional average of many such low-speed events reveals the presence of an elongated low-speed streak with counter-rotating vortices on either side of it. Similar thresholding techniques to extract features from turbulent flow fields in pipe, channel, or boundary layer flows, although for large-scale motions, have been adopted by Dennis and Nickels [73] and Lee and coworkers [74–76].

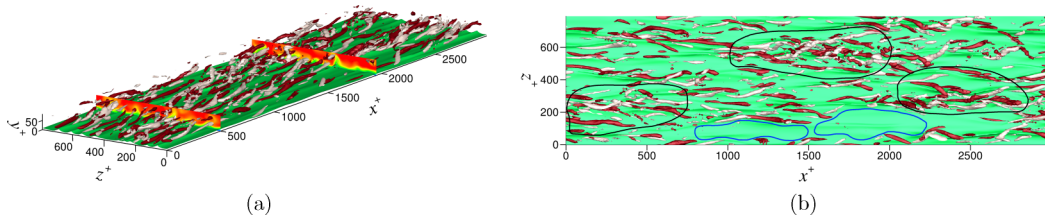


FIG. 2. Flow structures of a typical snapshot from channel flow DNS ($\text{Re}_\tau = 85$, $L_x^+ \approx 3000$, $L_z^+ \approx 800$). Flow is in the x direction. Only the lower half of the channel is shown. The green sheet is the isosurface of streamwise velocity $U = 0.35$; cross planes [(a) view from an angle] at $x^+ = 500$ and 1950 show contours of streamwise velocity; tubular structures are isosurfaces of $Q_{2D} = 0.05$ [38] color-coded by the streamwise vorticity at the same location: Red represents positive vorticity and white represents negative vorticity. Sample regions showing weak and strong fluctuations are shown enclosed by blue and black boundaries, respectively [(b) view from top].

For the most part, the work just described does not address the question introduced above regarding the relationship between temporal intermittency in minimal domains and spatiotemporal intermittency in extended ones. Indeed very little study has been made of the dynamics of the laminar intervals in laminar-turbulent transition, although the dynamics in these regions can be nontrivial and according to Avila *et al.* [77] persist into the fully turbulent regime. Evidence for the existence of a spatiotemporal relationship between minimal channels and full turbulent flows has been presented by Jiménez and coworkers [78–80]. They have shown that the variability in temporal statistics during bursting events in minimal boxes agrees well with the variability in spatial statistics in sub-boxes of similar sizes in large domains, suggesting that the flow dynamics in minimal channels are also part of full-size turbulent flows. Figure 2 shows a snapshot from a channel flow DNS in which we have arbitrarily circled regions of intense or weak turbulence activity (regions of active and hibernating turbulence in the nomenclature introduced in Ref. [39]). The aim of the present work is to systematically characterize the dynamics and structure in these regions and examine their relationship to minimal channel and ECS results.

The paper is organized as follows. A brief discussion on formulation of the system and simulation parameters are presented in Sec. II. Sampling methodology of intermittent low- and high-drag events based on pointwise sampling of wall shear stress and conditional averaging of these events are discussed in Sec. III A 1. In Sec. III A 2 we quantify this temporal intermittency. The mean velocity profiles of low- and high-drag intervals are presented in Sec. III A 3 and the underlying flow structures during these events have been illustrated in Sec. III A 4. Section III B 1 presents a discussion on the identification of spatial intermittency and a comparison of temporal statistics in a large domain with the spatial statistics, and finally in Sec. III B 2 we compare DNS results with nonlinear traveling-wave solutions and find connections between the two. A summary of main results and conclusions is presented in Sec. IV.

II. FORMULATION

We consider pressure driven flow of an incompressible Newtonian fluid in a rectangular, wall-bounded domain (channel) maintained at constant mass flux, a schematic of which is shown in Fig. 3. The x , y , and z axes correspond to the streamwise, wall-normal, and spanwise directions, respectively. No-slip boundary conditions are applied at the top and bottom walls and periodic boundary conditions are adopted in the streamwise and spanwise directions. The periods are L_x and L_z in these directions, respectively. The half-channel height $l = L_y/2$ is chosen as the characteristic length scale for nondimensionalization of all the lengths in the geometry. Velocities are scaled with the laminar centreline velocity U_c for the given mass flux. Time t is scaled with l/U_c and pressure

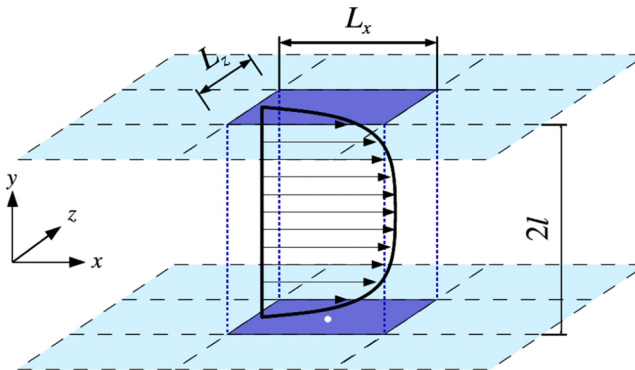


FIG. 3. Schematic of the plane Poiseuille flow geometry: The actual simulation box is highlighted with dark-colored walls in the center, surrounded by its periodic images. The white dot on the bottom wall represents a sampling point x_s , where we measure the instantaneous wall shear stress in Sec. III A.

p with ρU_c^2 , where ρ is the fluid density. The nondimensionalized Navier-Stokes equations are then given as

$$\frac{\partial \mathbf{u}}{\partial t} + \mathbf{u} \cdot \nabla \mathbf{u} = -\nabla p + \frac{1}{\text{Re}} \nabla^2 \mathbf{u}, \quad (1)$$

$$\nabla \cdot \mathbf{u} = 0. \quad (2)$$

The Reynolds number is given as $\text{Re} \equiv lU_c/\nu$, where ν is the kinematic viscosity of the fluid. The friction Reynolds number is defined as $\text{Re}_\tau \equiv lu_\tau/\nu$, where $u_\tau \equiv \sqrt{\overline{\tau_w}/\rho}$ is the friction velocity; $\overline{\tau_w}$ is the time- and area-averaged (mean) wall shear stress.

This study focusses on results for three Reynolds numbers, $\text{Re} = 1490, 1820, \text{ and } 2200$ (corresponding to friction Reynolds numbers, $\text{Re}_\tau = 70, 85, \text{ and } 100$, respectively). The streamwise and spanwise periods in outer units are $42.86l \times 11.43l$ at $\text{Re}_\tau = 70$, $35.36l \times 9.43l$ at $\text{Re}_\tau = 85$, and $30.00l \times 8.00l$ at $\text{Re}_\tau = 100$. These dimensions correspond to a domain size of $L_x^+ \approx 3000$, $L_z^+ \approx 800$ in wall units at all values of Re_τ : 70, 85, and 100. Here, the superscript $+$ indicates normalization with the viscous length scale, $\delta_v = \nu/u_\tau$.

Simulations are performed using ChannelFlow, a direct numerical simulator for incompressible Newtonian fluid flow in a periodic, rectangular, wall-bounded domain, developed and maintained by Gibson [81]. The system of coupled equations (1) and (2) is integrated in time with a third-order semi-implicit scheme: A third-order implicit backward differentiation method is used to update the linear terms while the nonlinear terms are integrated with an explicit third-order Adams-Bashforth method [82]. Fourier-Chebyshev-Fourier spatial discretization is applied in all variables and nonlinear terms are calculated with the collocation method. We use $(N_x, N_y, N_z) = (196, 73, 164)$ grid points for $\text{Re}_\tau = 70$, $(160, 73, 120)$ grid points for $\text{Re}_\tau = 85$ and $(160, 85, 120)$ grid points for $\text{Re}_\tau = 100$ in the streamwise, wall-normal, and spanwise directions, respectively. The numerical grid spacings in streamwise and spanwise directions are $\delta_x^+ \approx 15$ and $\delta_z^+ \approx 5$, respectively, for all the cases. Nonuniform Chebyshev spacing in the wall-normal direction gives $\delta_{y,\text{min}}^+ \approx 0.07$ at the wall and $\delta_{y,\text{max}}^+ \approx 3$ at the center of the channel. A constant time step, $\delta t = 0.02$, which satisfies the CFL stability condition, is used in all simulations. The spatial and temporal resolutions are at the same level as those reported in previous studies [83]. A convergence check was also done—spatial resolution was increased and all the quantities reported in the paper were recalculated, yielding negligible changes from the results reported here. Each simulation run is sufficiently long (more than $25\text{Re} \approx 6 \times 10^4 l/U_c$ time units) to ensure meaningful statistical averages.

III. RESULTS AND DISCUSSION

The results are organized as follows. In Sec. III A we characterize events based on temporal behavior—the fundamental measurement we consider here is the time series of shear stress at a point on the wall. Based on behavior, specifically low- and high-drag events at that point, we focus on the time series of flow properties at a point on a wall and at various discrete distances above the wall, flow properties are sampled conditionally based on when an event happens in time, and conditional averages are presented. In Sec. III B we characterize events based on space. Instead of focusing just at a point, we examine the entire domain at the same time. Spatial regions or patches showing similar characteristics are identified and put together in order to get spatially conditional averages. Finally, we compare temporal and spatial dynamics of large-domain DNS with minimal channel ECS.

A. Temporal intermittency

1. Time series of wall shear stress—unconditional and conditional

We first describe our method of characterization of events with varying amounts of drag relative to the mean. To detect and sample such events happening locally with time, we measure the instantaneous wall shear stress at a sampling point \mathbf{x}_s on a wall. A point \mathbf{x}_s is shown as a white dot on the bottom wall in Fig. 3. In fact, to get better statistics we choose nine measurement locations on the wall of the large domain in a way that the shear stress at each location is not correlated with the other locations: Any two adjacent points are 1.67×2.67 correlation lengths apart. Our criteria for an event is that the wall shear stress (τ_w) at \mathbf{x}_s must pass through a threshold value and stay on the same side of the threshold for a specified minimum time duration. Specifically, for a hibernation event, characterized by low drag, the wall shear stress must fall below the specified threshold and remain below it for a specified time duration, and likewise for a high-drag hyperactive event where τ_w must exceed a threshold value for a specified duration. We measure this time duration in units of $t^* = t u_\tau / l$, i.e., eddy turnover times, and our base case is to set this duration to $t^* = 3$ —we address below the issue of sensitivity to the chosen value while for the moment we note that this value was chosen based on observations from prior work. Jiménez and Moin [43] have observed that the peak-to-peak distance in the time series of wall-shear deviations from the mean in turbulence in a minimal channel is about $t^* \approx 4$. Similar observations were made in MFUs by Webber *et al.* [84]. Xi and Graham [39] defined hibernation in minimal channels as events when the area-averaged wall shear stress is below 90% of its mean value for more than $1.18t^*$. In a later study [42] in which hibernation was defined differently, they showed that the average duration of hibernation events was $t^* \approx 4.5$. The default threshold values chosen for the current study are 90% of the mean wall shear stress ($\overline{\tau_w}$) for a hibernation event and 110% of $\overline{\tau_w}$ for a hyperactive event. For $\text{Re}_\tau = 70, 85, 100$, $t^* > 3$ corresponds to $t U_c / l > 63.5, 64.5, 65.3$, respectively, in outer units and $t u_\tau^2 / \nu > 211.1, 254.1, 303.1$, respectively, in inner units. Again, sensitivity to the threshold value is addressed with the presentation of the results.

Figure 4 shows time series of shear stress measured at a point \mathbf{x}_s at $\text{Re}_\tau = 70, 85$, and 100. By the criteria above, the flow is in hibernation during the intervals bounded by the vertical orange lines: The instantaneous wall shear stress (gray line) is significantly lower than the time averaged value ($\overline{\tau_w}$) shown as a dashed line for 3 or more l/u_τ . These are examples of low-drag events in turbulence and this intermittent behavior is observed at all the Reynolds numbers considered. Figure 5 shows some instantaneous snapshots of wall shear stress fluctuations before and during hibernation events at friction Reynolds numbers 70, 85, and 100. The white dot in the center of the domain represents the location where the wall shear stress shown in Fig. 4 is measured. The flow structures are significantly three-dimensional at all the Reynolds numbers considered and fluctuations can be seen throughout the domain: The intermittency observed is purely *within* turbulence. It is interesting to note that at $\text{Re}_\tau = 70$, which is the lowest Re_τ we consider, a large-scale structure of weak and strong turbulent fluctuations appears in the form of stripes that are oriented obliquely relative to the mean flow. Similar stripy patterns have also been observed experimentally in channel flow by Hashimoto *et al.* [60]

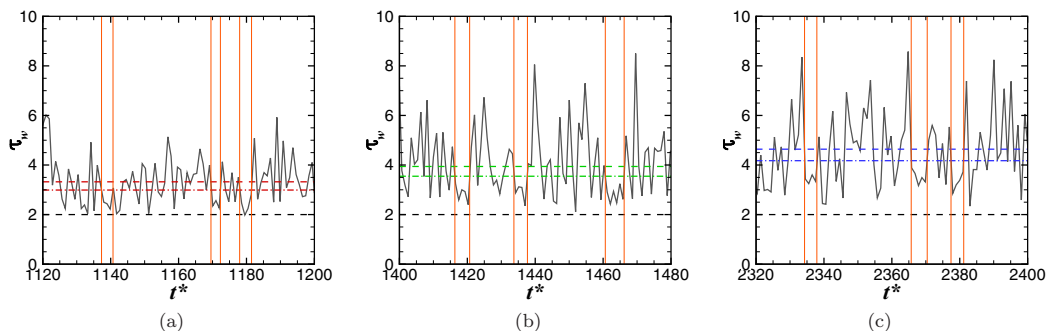


FIG. 4. Time series of the wall shear stress at different friction Reynolds numbers. Gray, instantaneous; black dashed, laminar; color dashed, time averaged; color dashed-dotted, threshold. (a) $Re_\tau = 70$, (b) $Re_\tau = 85$, and (c) $Re_\tau = 100$.

as well as in Couette flow computations (e.g., Ref. [63]). The stripes we see here are oriented at $20\text{--}30^\circ$ relative to the mean flow, which is in excellent agreement with the orientation angle reported in experiments [60]. As the Reynolds number increases, the stripiness start to disappear [see Figs. 5(c)–5(f)] and eventually the turbulence becomes uniform. Further, it can be observed that in the before hibernation figures (left column), the wall shear stress at and near the measurement point is high (red), whereas it is low (blue) in the after hibernation figures (right column).

In Fig. 6(a), we show time series of 639 temporal hibernation events measured at $Re_\tau = 85$. The beginning of each event is shifted to $t^* = 0$. The ensemble average of all the instantaneous hibernation

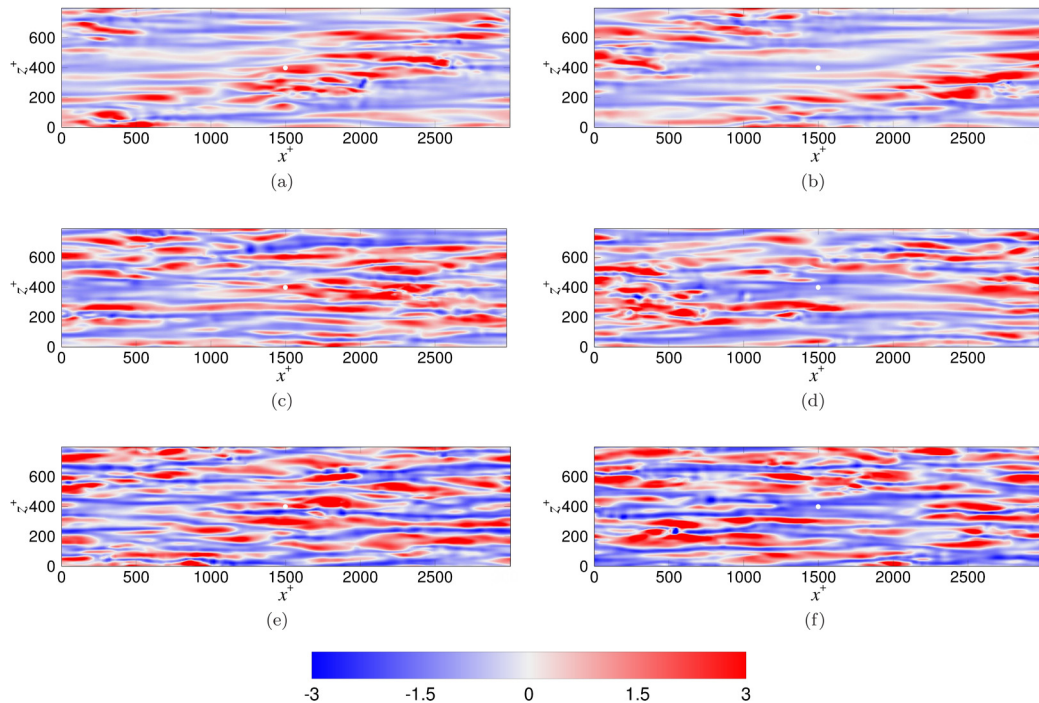


FIG. 5. Spatial patterns of instantaneous wall shear stress fluctuations in the x - z plane of a turbulent channel flow at [(a), (b)] $Re_\tau = 70$, [(c), (d)] 85, and [(e), (f)] 100. Figures in the left column show patterns before hibernation, and figures in the right column depict patterns during hibernation.

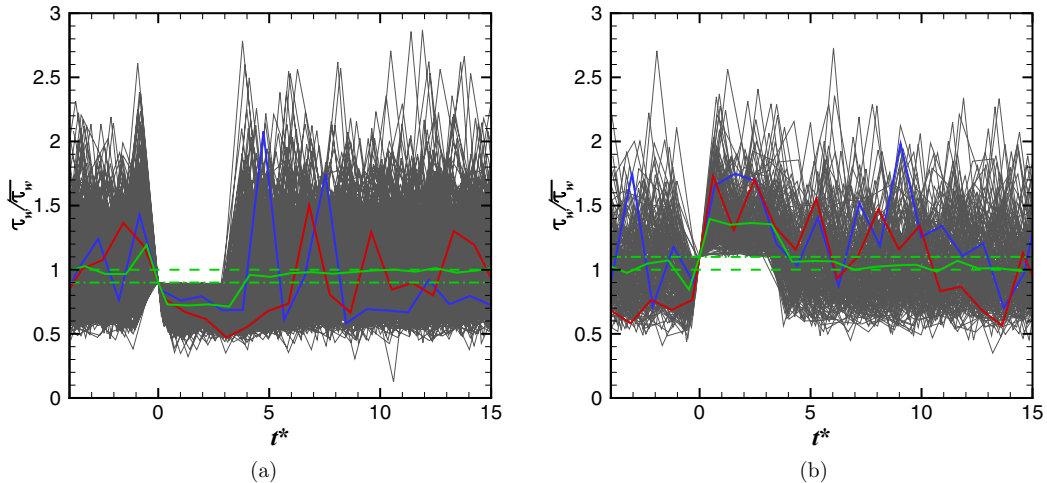


FIG. 6. Instantaneous (thin gray lines) and ensemble-averaged (thick green solid line) wall shear stress before, during, and after the intervals of (a) hibernation and (b) hyperactivity at $Re_\tau = 85$. The thick blue and red lines highlight specific individual instantaneous events with a duration of 4 and 6 eddy turnover times, respectively. The mean wall shear stress is represented by the green dashed line and the threshold by the green dashed-dotted line. All the events are shifted along the time axis such that $t^* = 0$ represents their beginning.

events is shown as a thick green line. On average, the wall shear stress during hibernation falls to a plateau in the time interval $0.7 \leq t^* \leq 3.0$ and is preceded by a sharp peak in the wall shear stress (higher than the mean) during $-0.8 \leq t^* \leq 0$. Figure 6(b) shows instances that satisfy the hyperactivity criterion. Before hyperactivity begins, a brief drop in the wall shear stress is observed and it becomes higher than the mean for $t^* \approx 0.7-3.0$. The frequency of occurrence of hibernation and hyperactive events has been quantified and the results are presented in Sec. III A 2. We do not yet have a physical explanation as to why there is a spike in wall shear stress before hibernation or a dip before hyperactivity.

The above-mentioned characteristics of hibernation and hyperactivity are observed for a range of Reynolds numbers studied ($Re_\tau = 70, 85, 100$). Figure 7(a) shows ensemble-averaged wall shear stress before, during, and after hibernation for three different Reynolds numbers. Error bars representing standard error of the data at their respective Reynolds number are also shown. The error bars are small, especially within the low-drag events.

As the Reynolds number is increased, keeping the threshold the same, the decrease in wall shear stress during hibernation events becomes larger. This claim is supported by the observation that the standard error during hibernation events is smaller than the variation in the wall shear stress observed with increasing Re_τ . On the other hand, the effect of Reynolds number on the strength of hyperactive turbulence is not very clear, as shown in Fig. 7(b), although a drop in wall shear stress before the start of hyperactivity is still observed for all the cases.

Figure 8 illustrates what happens to the wall shear stress as flow leaves hibernation. Here, data from Figs. 6(a) and 7(a) are replotted with the time axis shifted such that $t^* = 0$ represents the *end* of a hibernation event. We observe that on average, as the flow leaves hibernation, there is a brief spike in the wall shear stress. This effect is observed at all Reynolds numbers considered. As seen earlier in Fig. 7(a), the strength of hibernation increases with Reynolds number.

A detailed sensitivity analysis at $Re_\tau = 100$, showing the effect of both threshold and time duration criteria on the stress plateau just after the beginning of hibernation, is presented in Fig. 9. It is observed in Fig. 9 that as the threshold criterion for hibernation is made more stringent, i.e., going from 95% to 75% of the mean stress, the stress during hibernation becomes smaller, but for a constant threshold, the stress plateau remains the same for both the durations, indicating that the

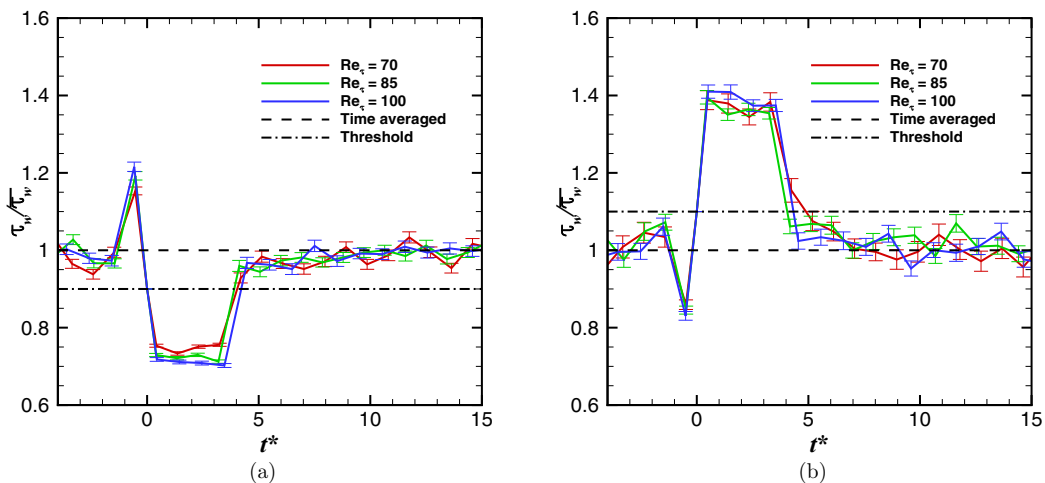


FIG. 7. Ensemble-averaged wall shear stress before, during, and after hibernation and hyperactivity at different Reynolds numbers along with the mean and sampling threshold values. Error bars indicate standard error. Here $t^* = 0$ corresponds to the beginning of an event. (a) Hibernation: threshold $\tau_w/\overline{\tau_w} \leq 90\%$ and (b) hyperactivity: threshold $\tau_w/\overline{\tau_w} \geq 110\%$.

cutoff duration has no effect on the strength of hibernation. Results for the exit from hibernation as well as for hyperactivity are analogous, as are those at $\text{Re}_\tau = 70$ and 85. Thus, for brevity, they are omitted.

2. Statistics of temporal events

In this section we quantify the duration and frequency of occurrence of hibernating and hyperactive turbulence and their dependence on Reynolds number. The statistics reported in this section are obtained from simulation runs over a duration of $60000 l/U_c$ (more than 25Re) for all the cases.

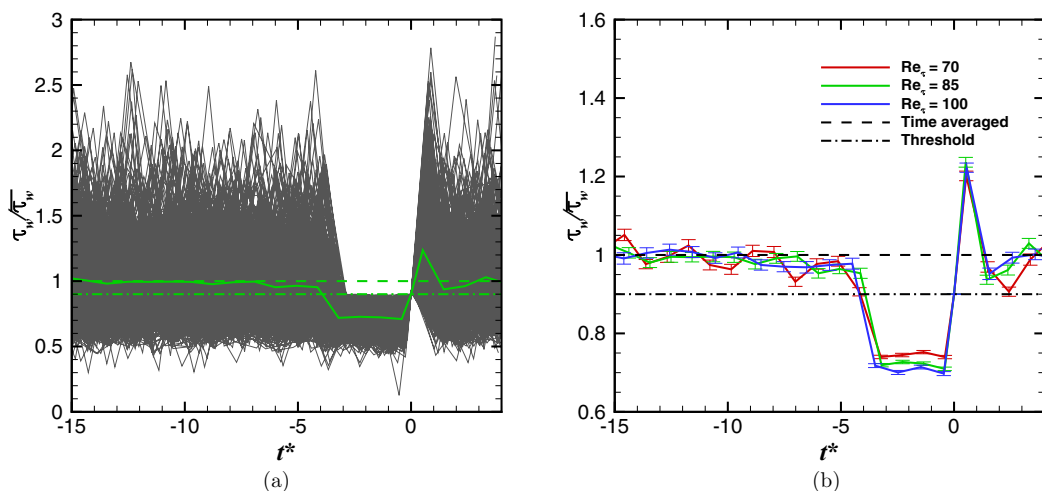


FIG. 8. (a) Instantaneous and ensemble-averaged wall shear stress at $\text{Re}_\tau = 85$ and (b) ensemble-averaged wall shear stress at different Reynolds numbers as the flow leaves hibernation. Error bars indicate standard error. Here $t^* = 0$ corresponds to the end of an event.

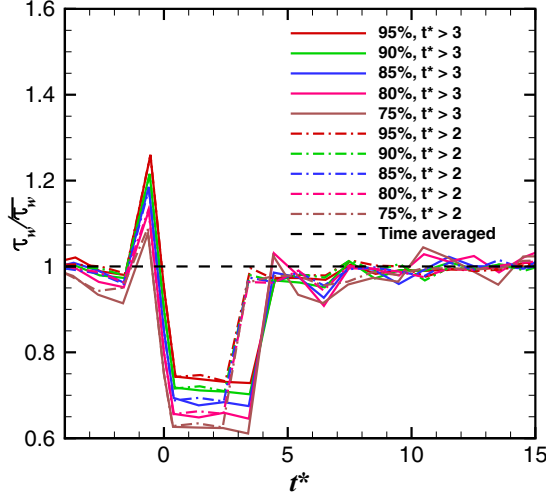


FIG. 9. Conditional wall shear stress for start of hibernation at $Re_\tau = 100$. Results are presented for various threshold criteria (95%, 90%, 85%, 80%, 75%—increasing hibernation strictness in that order) and time durations ($t^* > 3$ and $t^* > 2$). Error bars are not shown to avoid overcrowding. Here $t^* = 0$ corresponds to the beginning of a hibernation event.

The average duration of hibernating events is calculated as

$$\overline{t_H} = \frac{\sum_{n=1}^{N_H} t_{H,n}}{N_H}, \quad (3)$$

where $t_{H,n}$ is the duration of the n th hibernating interval and N_H is the total number of hibernating intervals identified in the data set. On similar lines, we can define temporal intermittency factors for hibernation and hyperactivity, specifically, the fraction of time flow spends in hibernation and hyperactivity, respectively. These intermittency factors are calculated as

$$F_H = \frac{\sum_{n=1}^{N_H} t_{H,n}}{T}, \quad (4)$$

$$F_{HA} = \frac{\sum_{n=1}^{N_{HA}} t_{HA,n}}{T}. \quad (5)$$

Here, F_H and F_{HA} are temporal intermittency factors for hibernation and hyperactivity, respectively, $t_{HA,n}$ is the duration of the n th hyperactive interval, and T is the total duration of the simulation. Note that $F_H + F_{HA} < 1$ because for the major part of the total time the flow is neither in hibernation nor in hyperactivity. The quantities calculated from above equations are plotted in Fig. 10, illustrating their dependence on Reynolds number.

We observe that the fraction of time spent in hibernation, F_H , decreases with increase in Reynolds number. In contrast, the average duration of hibernating intervals remains almost invariant with the change in Re_τ : It is a bit higher than the cutoff duration chosen for the identification of hibernating or hyperactive events, i.e., $t^* = 3$. The average duration of hyperactive events, $\overline{t_{HA}}$, was also calculated using an expression analogous to Eq. (3) and it was found to be very similar to $\overline{t_H}$ (hence not plotted to avoid overcrowding). Since 3 is the minimum duration for hibernation and hyperactivity, their average duration must be larger than 3. The fraction of time spent in hyperactivity, F_{HA} , increases with increasing Re_τ . With the average duration of hibernation and hyperactivity remaining almost invariant with Reynolds number, and the corresponding time fraction decreasing and increasing, respectively, the following inferences can be drawn for hibernating and hyperactive turbulence.

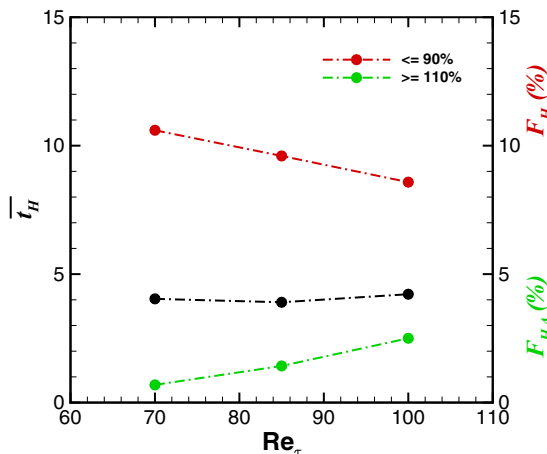


FIG. 10. Average duration of hibernating turbulence (left ordinate) and the fraction of time spent in hibernation and hyperactivity, F_H and F_{HA} , respectively, (right ordinate) as functions of friction Reynolds number.

Increasing the Reynolds number and/or the strictness of the threshold criterion makes hibernation happen less frequently. Second, the frequency of occurrence of hyperactive turbulence decreases with the threshold, whereas it increases with the Reynolds number.

It is important to note that the above-mentioned quantities, \bar{t}_H , F_H , $\overline{t_{HA}}$, and F_{HA} , should be interpreted in terms of their behavior and trend with respect to Re_τ and the threshold; their specific values will definitely depend on the choice of the cutoff duration for a hibernating/hyperactive event. For example, if we choose $t^* = 2.5$ as the criterion for a hibernating/hyperactive event, \bar{t}_H and $\overline{t_{HA}}$ decrease and F_H and F_{HA} increase. Nevertheless, the overall trends remain similar to the $t^* = 3$ case. It is also worth noting that the occurrence of hyperactive events is in general very infrequent—all the cases reported are less than 5%, and they become extremely rare at low Reynolds numbers ($< 1\%$).

It is worth mentioning that the finite box size does seem to have some effect on intermittency factors: We calculated the same quantities for a box 1.7 times bigger in both streamwise and spanwise directions and found that both F_H and F_{HA} have reduced. Their trend as a function of Re_τ remains the same, however. On the other hand, it should also be noted that the *conditional* quantities including wall shear stress (including the precursor peak and plateau), mean velocity, and flow structures, are insensitive to a further increase in box size.

3. Conditional mean velocity profiles

Figure 11 shows the streamwise unconditional time-averaged velocity profiles at different Reynolds numbers with solid lines. These all lie slightly above the Prandtl–von Kármán log-law and are in good agreement with experimental and other numerical values reported in the literature at similar Reynolds numbers [85–87]. In Fig. 11(a) we also present in solid circles the conditional mean velocity profiles during hibernation events at the same Reynolds numbers, evaluated on a line extending from the measurement point x_s vertically into the fluid. These profiles are calculated by first determining the ensemble-averaged streamwise velocity for several hibernation events, averaging it over the plateau region $t^* = 0.7$ – 3.0 , and finally scaling it with the hibernating wall shear stress determined during the same time interval. For reference, also shown on the same plot is the 95% confidence interval to the MDR asymptote within which velocity profiles in the MDR regime from a number of representative computational and experimental studies lie [89]—close to the wall, data for polymer solutions lie close to the lower end of the interval, while farther from the wall it approaches the upper end. The hibernating profiles lie well above the Prandtl–von Kármán log-law, and in fact

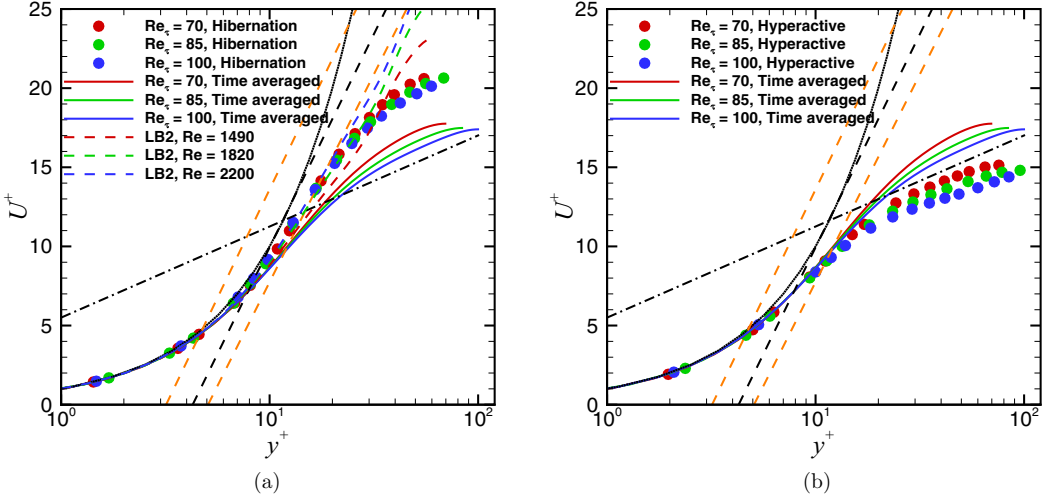


FIG. 11. Unconditional (solid lines) and conditional (filled circles) ensemble-averaged streamwise mean-velocity profiles at different Reynolds numbers. The black dotted line is the viscous sublayer, $U^+ = y^+$; black dashed-dotted line is the Prandtl–von Kármán log-law, $U^+ = 2.5 \ln y^+ + 5.5$; and the black dashed line is the Virk MDR log-law, $U^+ = 11.7 \ln y^+ - 17.0$. The orange dashed lines show the lower and upper 95% confidence intervals to the MDR asymptote [88,89]. (a) Hibernation: threshold $\tau_w/\bar{\tau}_w \leq 90\%$ and (b) hyperactivity: threshold $\tau_w/\bar{\tau}_w \geq 110\%$.

brush against the lower end of the MDR confidence interval. Figure 11(a) also shows mean velocity profiles of lower branch ECS. It is observed that in the region $y^+ \lesssim 30$ the conditional and ECS velocity profiles are very similar while close to the centreline the conditional turbulent mean deviates downward from the ECS profile. Even in the low-drag intervals the turbulence has fluctuations in the core of the flow that are absent from the P4 lower branch solutions. Only a weak dependence of conditional profiles on Re_τ is observed.

Mean velocity profiles during hyperactive turbulence are illustrated in Fig. 11(b), alongside the unconditional profiles at the same Reynolds numbers. It is observed that as the Reynolds number is increased keeping the threshold criterion fixed, the mean velocity profile of the hyperactive event moves down, away from the Prandtl–von Kármán log-law.

A detailed sensitivity analysis at $Re_\tau = 100$, showing the effect of both threshold and time duration criteria on the velocity profiles, is presented in Fig. 12. Increasing the strictness of the stress threshold (different colored curves) results in the lowering of the plateau stress during hibernation (Fig. 9), which then results in the elevation of velocity profile in the region $y^+ \gtrsim 20$ as shown in Fig. 12. Note that here also, and in all the future sections, each velocity profile is scaled with the corresponding mean wall shear stress, unconditional or conditional as the case may be. On the other hand, the velocity profiles are insensitive to the time duration (circles and triangles)—this result is consistent with with insensitivity of the stress plateau during hibernation on the duration threshold. The same trends are obtained for $Re_\tau = 70$ and 85.

4. Spatial variation of wall shear stress and flow structures during temporal hibernation events

In this section we look at the spatial patterns of wall shear stress and velocities observed before and during hibernation intervals. In particular, flow behavior at and away from the measurement location and its relation to hibernation and hyperactivity are discussed. Figures 13(a) and 13(b) show the spatial structure of ensemble-averaged wall shear stress fluctuations at $Re_\tau = 85$ before ($t^* = -0.52$) and during ($t^* = 0.41$) the hibernation event as observed at the white dot at the wall at $(x^+, z^+) = (1500, 400)$. They are generated by identifying several instantaneous hibernation events

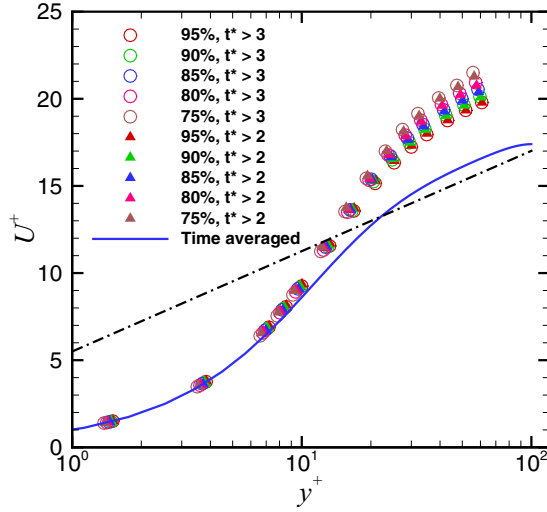


FIG. 12. Unconditional (line) and conditional (symbols) mean velocities for hibernation at $Re_\tau = 100$. Results are presented for various threshold criteria (95%, 90%, 85%, 80%, 75%—increasing hibernation strictness in that order) and time durations ($t^* > 3$ and $t^* > 2$).

at the center of the domain (white dot) based on the set criteria, $\tau_w/\overline{\tau_w} \leq 90\%$ for a duration of $t^* > 3$ for this case, shifting the time axis so that $t^* = 0$ corresponds to the time of the onset of hibernation, i.e., when the wall shear stress starts to fall below the threshold, and finally ensemble-averaging all the conditionally sampled instantaneous wall shear stress-fluctuation fields, $\tau'_w(x, z, t)$, corresponding to the given time. Here, the fluctuating field is given as $\tau'_w = \tau_w - \overline{\tau_w}$. Ensemble-averaged results at $Re_\tau = 70$ and 100 are qualitatively similar and hence not shown. The before picture [Fig. 13(a)] shows a region of higher-than-mean wall shear stress (red color) that corresponds to the precursor peak in the local wall shear stress as observed in Fig. 6(a). It also shows a region of lower-than-mean wall shear stress (blue color) trailing behind the red region. This blue region has fully developed in the after picture [Fig. 13(b)] and it corresponds to the plateau in the local wall shear stress in Fig. 6(a), depicting the low-wall shear stress nature of hibernating turbulence, for example, an elongated low-speed streak spanning a length of approximately 1500 and 50 viscous wall units in the streamwise and spanwise directions, respectively. This low-speed streak is a result of a low wall shear stress region and corresponds to a localized pair of counter-rotating vortices. The structures of these vortex pairs is discussed below. Sample instantaneous wall shear stress fluctuation fields before and during hibernation are shown in Fig. 5. In all the before pictures (left column) we can

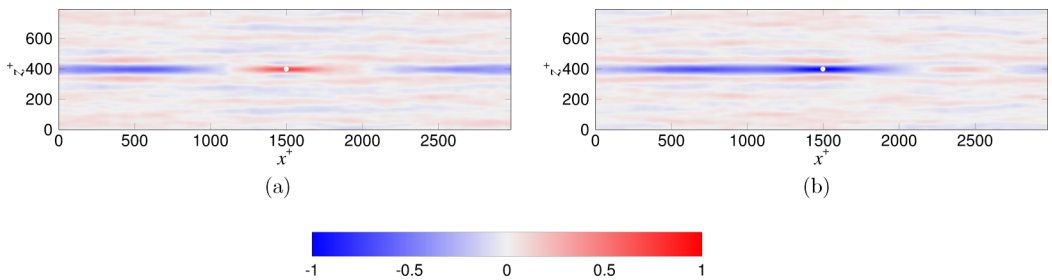


FIG. 13. Spatial patterns of ensemble-averaged conditionally sampled ($\tau_w/\overline{\tau_w} \leq 90\%$) wall shear stress fluctuations at $Re_\tau = 85$ (a) before ($t^* = -0.52$) and (b) during ($t^* = 0.41$) hibernation.

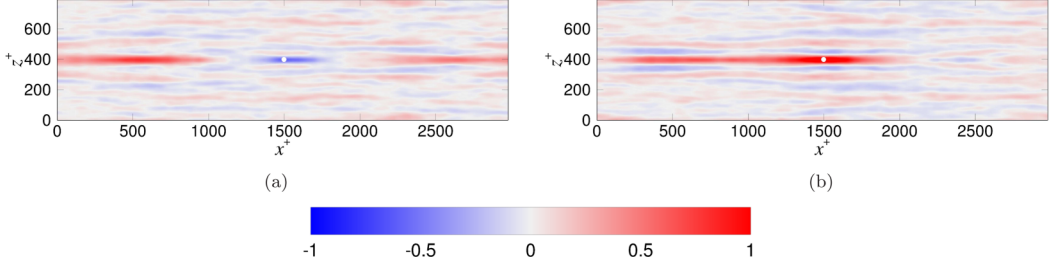


FIG. 14. Spatial patterns of ensemble-averaged conditionally sampled ($\tau_w/\overline{\tau_w} \geq 110\%$) wall shear stress fluctuations at $\text{Re}_\tau = 85$ (a) before ($t^* = -0.48$) and (b) during ($t^* = 0.45$) hyperactivity.

see high wall shear stress at the measurement location while in the after pictures (right column), a low wall shear stress is seen at the same location.

We use the method described above to generate the ensemble-averaged spatial patterns of the wall shear stress before and during hyperactivity. The light blue color in the center of Fig. 14(a) corresponds to the very brief drop in the wall shear stress before the start of hyperactivity; for example, see Fig. 6(b). The red region trailing behind it which is fully developed in the channel center [Fig. 14(b)] corresponds to the higher-than-mean wall shear stress during hyperactivity. As discussed in Sec. III A 2, the frequency of occurrence of hyperactive events is very low—only about 2% of the total time is spent in hyperactivity for the case plotted. Thus, averaging in even very long trajectories does not give good statistics. This effect can in fact be observed at points far from the measurement location in Fig. 14 where the wall shear stress does not revert as smoothly as in the case of low-drag events back to the overall mean value.

We now look at the spatial patterns at $\text{Re}_\tau = 85$ as the flow leaves hibernation. In Fig. 8(a) we observed a brief spike in the wall shear stress just after the hibernation period. The plateau of low wall shear stress is illustrated by an elongated low-speed streak in Fig. 15(a) and the spike that follows by a region of elevated wall shear stress at the measurement location in the center in Fig. 15(b).

We now look at the flow structures in the cross-flow plane as observed before and during hibernating intervals. In Fig. 16 we show the ensemble-averaged y - z planes of the channel at $\text{Re}_\tau = 85$ before ($t^* = -0.52$) the hibernation event. Figure 16(b) corresponds to the location where measurements are taken, at $x^+ = 1500$, while Fig. 16(a) corresponds to $x^+ = 500$, a region developing behind the measurement location. Flow is out of the plane. Contours represent the streamwise velocity whereas arrows represent the wall-normal and spanwise velocities.

At the measurement location we observe a downward motion of fluid (indicated by downward-pointing arrows) and this momentum transfer toward the wall results in a region of high wall shear stress corresponding to the precursor peak in Figs. 6(a) and 13(a). The low wall shear stress region that trails behind the high wall shear stress is formed due to the motion of fluid away from the wall.

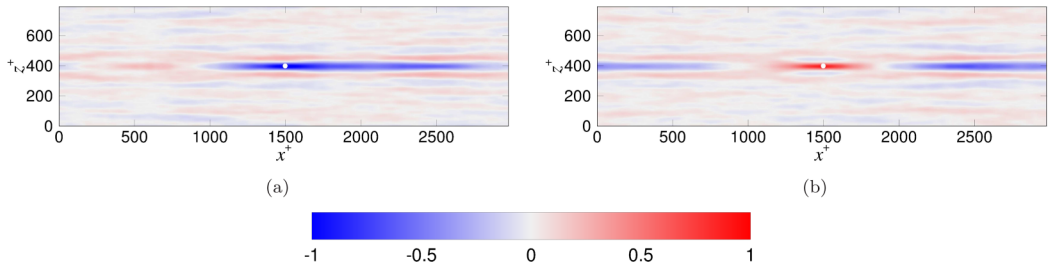


FIG. 15. Spatial patterns of ensemble-averaged conditionally sampled ($\tau_w/\overline{\tau_w} \leq 90\%$) wall shear stress fluctuations at $\text{Re}_\tau = 85$ (a) during ($t^* = -0.41$) and (b) after ($t^* = 0.52$) hibernation.

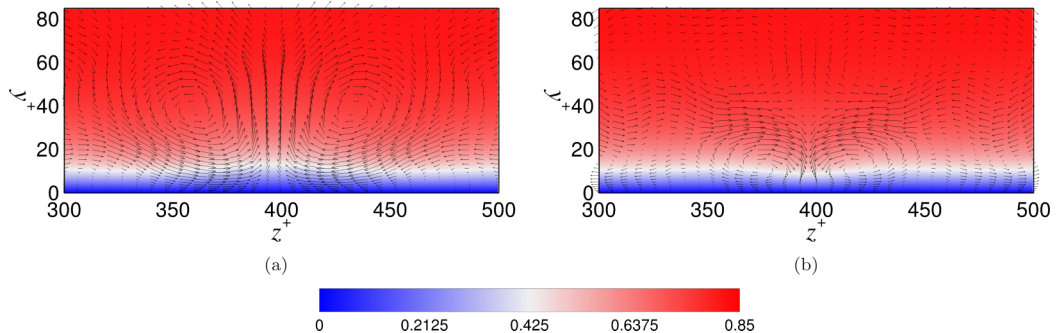


FIG. 16. Flow patterns of ensemble-averaged conditionally sampled ($\tau_w/\overline{\tau_w} \leq 90\%$) velocities in the y - z plane of a turbulent channel flow at $\text{Re}_\tau = 85$ *before* the hibernation event. (a) $x^+ = 500$ and (b) $x^+ = 1500$.

This region develops into a long low-speed streak as the flow enters hibernation. This is illustrated in Fig. 17 for $\text{Re}_\tau = 85$ at $t^* = 0.41$. At both the locations, i.e., measurement location at $x^+ = 1500$ and trailing location at $x^+ = 500$, we observe transfer of momentum away from the wall which corresponds to counter-rotating streamwise vortex pairs that result in a long streamwise streak as observed earlier in Fig. 13(b).

B. Spatial intermittency and connections with nonlinear traveling waves

1. Spatial distribution of hibernation and quantification of spatial intermittency

We now turn from temporal sampling to *spatial* sampling of the channel flow dynamics. To discriminate between spatially occurring high-, intermediate-, and low-drag regions and quantify the intermittency, we use a technique similar to what Nolan and Zaki [54] used to discriminate laminar spots from turbulent spots. Specifically, we introduce a detector function that uses information from longitudinal and lateral variations of velocity, and compute this for each snapshot obtained from DNS. Simply using the wall shear stress as the detector function is not desirable because even in a region of high turbulence activity there will be low-stress regions corresponding to low-speed streaks. We found that a better detector function combines the wall shear stress with the spanwise derivative of the streamwise velocity above the wall in the buffer layer:

$$D(x, z) \equiv \left| \frac{\partial U}{\partial y} \right|_w + \left| \frac{\partial U}{\partial z} \right|_{y^+=15}. \quad (6)$$

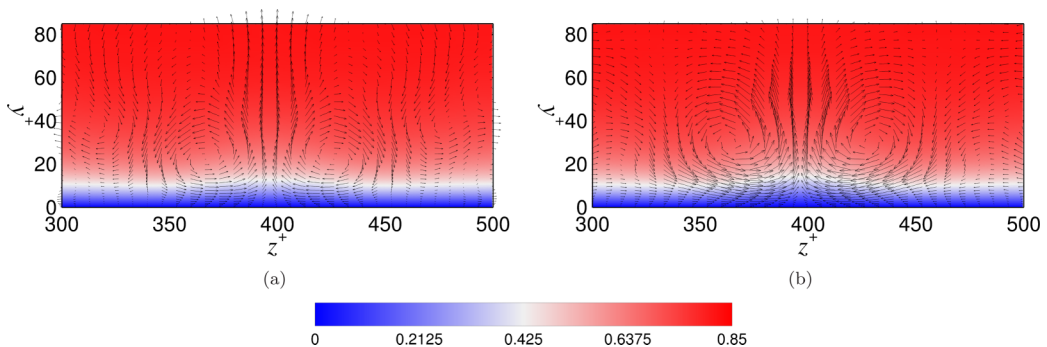


FIG. 17. Flow patterns of ensemble-averaged conditionally sampled ($\tau_w/\overline{\tau_w} \leq 90\%$) velocities in the y - z plane of a turbulent channel flow at $\text{Re}_\tau = 85$ *during* the hibernation event. (a) $x^+ = 500$ and (b) $x^+ = 1500$.

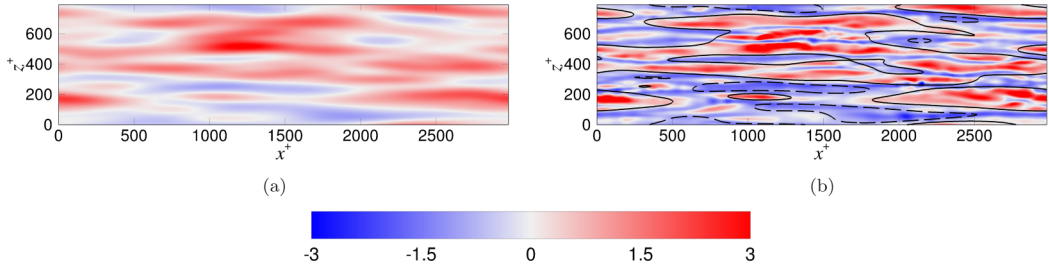


FIG. 18. Contours of (a) detector function after filtering and (b) spatial patterns of wall shear stress fluctuations from a single snapshot of DNS at $Re_\tau = 85$, along with the thresholds (solid and dashed curves) obtained from application of Otsu’s method to the field shown in (a).

The first term on the right-hand side is simply the drag; the reasoning for choosing the second term is as follows. It is known that the streaks do not always flow straight in the streamwise direction—they meander in the spanwise direction as well. Johansson *et al.* [90] showed that streaky structures asymmetric in the spanwise direction result in large turbulence production. To take this into account, we include the streamwise velocity gradient in the spanwise direction, $\partial U/\partial z$, in the buffer layer at the point of maximum variance, $y^+ = 15$, in our detector function. We did consider other detector functions, for example, $D = |\partial U/\partial y|_w + |\partial W/\partial y|_w$, where W is the spanwise velocity—both gave very similar results. This function is lowpass filtered by a Gaussian filter, the size of which is set according to correlation lengths: the characteristic streamwise length of the streak (600 wall units) and the characteristic stream spacing (100 wall units). We then apply Otsu’s method independently to the D field for each snapshot [69], which results in a demarcation between regions of varying levels of turbulence. We emphasize that there are no explicit thresholds of either time or stress level in Otsu’s method—all we specify is the number of classes we want the data at each time instant to be classified into. Otsu’s method picks out the optimum threshold by minimizing the *intra*class variance, or in other words, maximizing the *inter*class variance. We specify that three classes be sought (corresponding to low, intermediate, and high values of D). The boundaries (or edges) between any two classes results in demarcation of weakly, intermediately and strongly fluctuating regions (hibernating, active, and hyperactive).

An example of the result of the Otsu algorithm is shown in Fig. 18. The contours in Fig. 18(b) represent the wall shear stress patterns from an instantaneous flow field at $Re_\tau = 85$. Black solid and dashed lines correspond to the two thresholds obtained from the filtered detector function at the same time instant, the contours of which are shown in Fig. 18(a). The solid line represents the demarcation line between high-drag and intermediate-drag regions and the dashed line separates the intermediate-drag areas from the low-drag areas. A distinct difference between the three regions is observed—areas enclosed by solid lines show high wall shear stress and strong fluctuations whereas the areas enclosed by dashed lines are smooth, local wall shear stress values are low, and the variations are small. Regions between solid and dashed lines lie in the intermediate-drag regime.

Streamwise velocity profiles are sampled conditionally for the three intermittent spatial regimes—low, intermediate, and high D —and averaged over those conditional areas for the entire time series. Note that we are treating all the spatially occurring low-drag events equally—an event covering a large area is given equal weight as two or more widely separated events covering the same area. The same is applicable to intermediate- and high-drag events. In Figs. 19(a)–19(c) we compare conditionally averaged mean velocity profiles from edge-detection scheme with the pointwise thresholding results discussed earlier in Sec. III A 3. We see a clear dependence of mean flow statistics on the spatially intermittent nature of near-wall turbulence—the conditional profiles in the low- and high-drag regions lie, respectively, above and below the intermediate drag conditional profile, which lies almost over the unconditional time-averaged velocity profile. This is observed at all the Reynolds numbers. We also find a very good agreement of velocity profiles of hibernating, active, and hyperactive turbulence

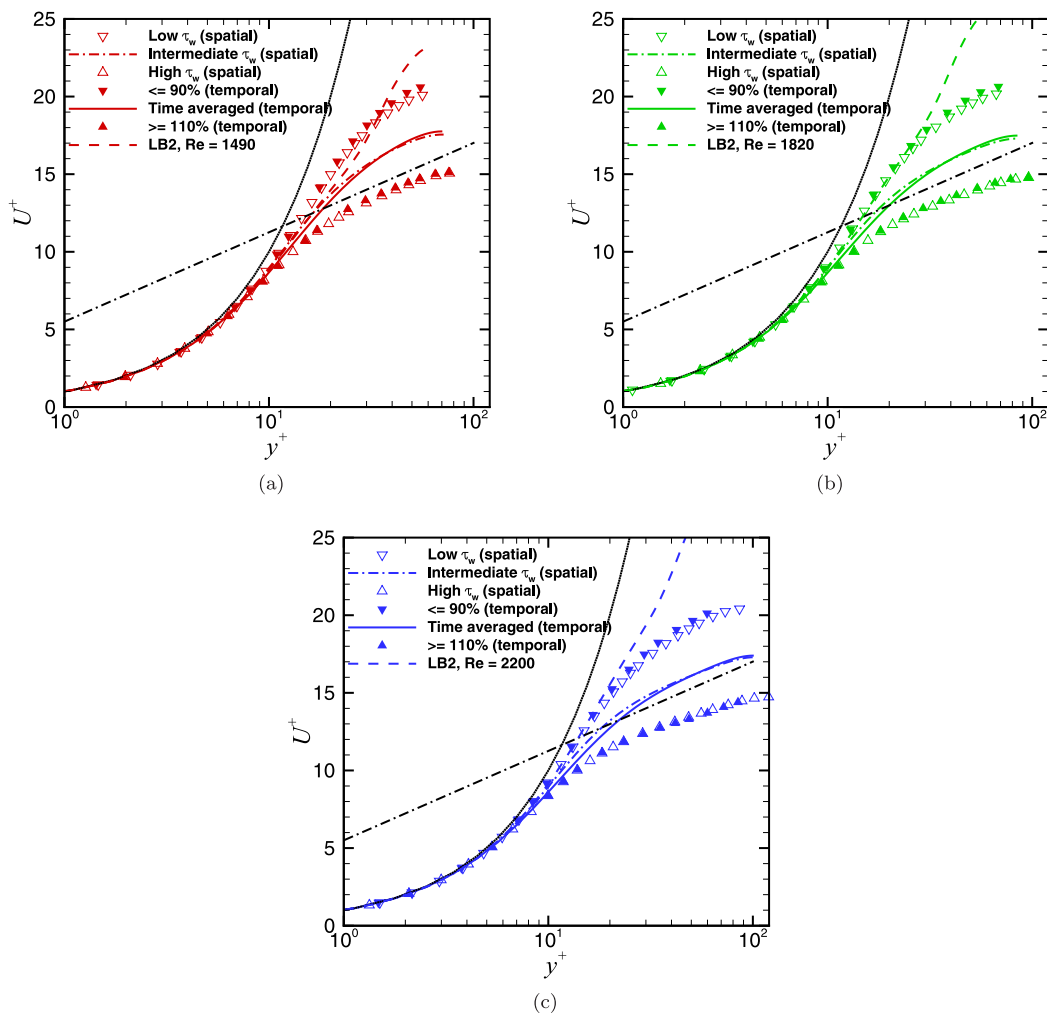


FIG. 19. A comparison between conditionally-averaged streamwise velocity profiles based on time and space criteria at the corresponding Reynolds number. (a) $Re_\tau = 70$, (b) $Re_\tau = 85$, and (c) $Re_\tau = 100$.

that were based on temporal analysis with those from spatial analysis; i.e., conditional low- and high-drag velocity profiles from temporal sampling show good correspondence with the conditional low- and high-drag profiles, respectively, from spatial analysis. It is important to emphasize that the temporal and spatial sampling techniques are completely different from one another (the temporal analysis requires thresholds on wall shear stress and time duration to be specified explicitly while there are no predetermined thresholds in the spatial analysis), so the quantitative similarity between the results is a reflection of the robustness of the intermittency phenomenon in these flows. Here also, the agreement between velocity profiles of lower branch ECS and low-drag regions is good in the region $y^+ \lesssim 30$, especially for $Re_\tau = 70$ and 85.

In the above results, we have illustrated the intermittent dynamics (both temporal and spatial) of transitional channel flow turbulence in an extended domain. In minimal channels, the intermittency is associated with the chaotic movement of turbulent trajectories between lower and upper branch ECS. In Fig. 20, we compare conditional mean profiles from our analyses here to those in the minimal channel. Velocity profiles of ECS are also included for comparison. The mean velocity profile of low drag events in the minimal channel is determined using the log-law slope criterion developed by Xi

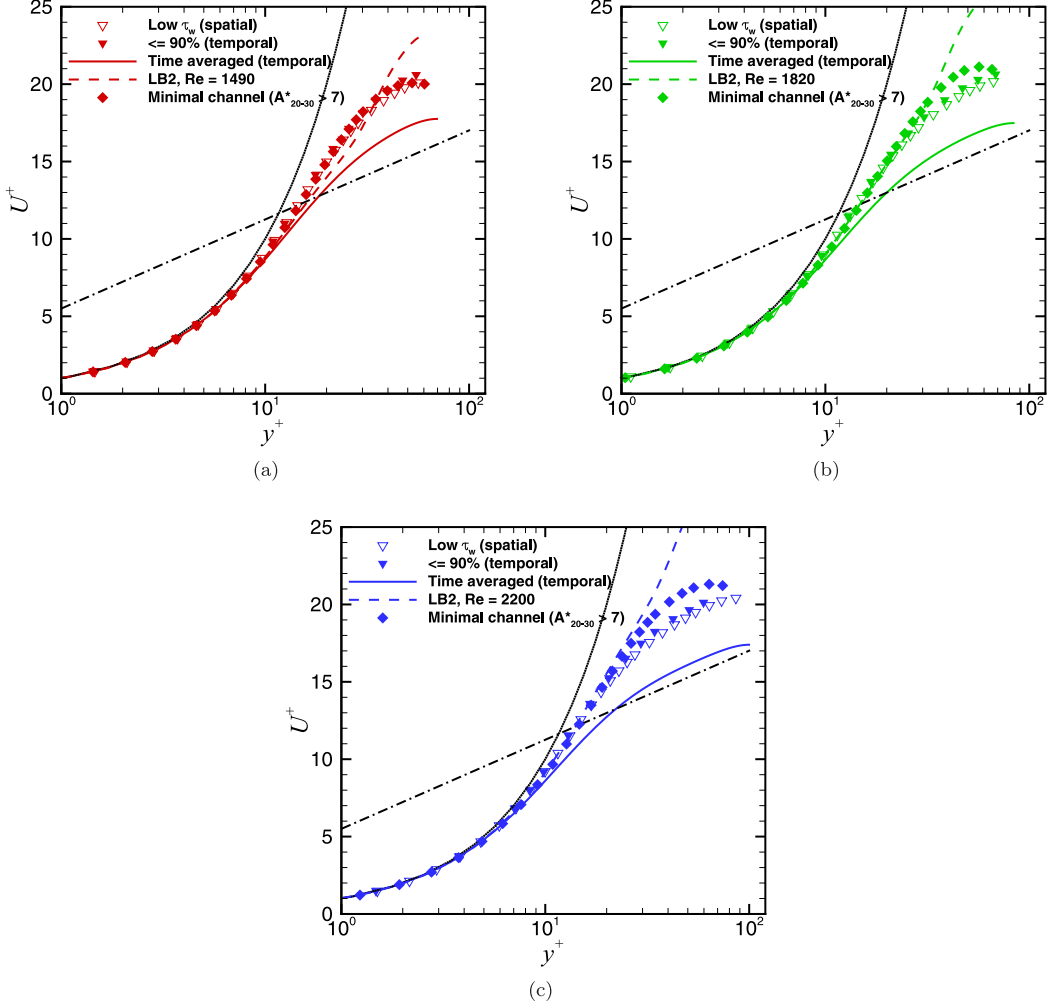


FIG. 20. Comparison of low-drag velocity profiles in minimal channel occurring temporally (when $A_{20-30}^* > 7$) with low-drag velocity profiles in an extended domain occurring both temporally (when $\tau_w/\bar{\tau}_w \leq 90\%$ for $t^* > 3$) and spatially [regions of low values of $D(x, z)$]. Velocity profiles of lower branch ECS are also plotted for comparison. (a) $Re_\tau = 70$, (b) $Re_\tau = 85$, and (c) $Re_\tau = 100$.

and Graham [42]: The instantaneous log-law slope of the velocity profile (A_{20-30}^*) is obtained in the interval $y^* = 20-30$, and if $A_{20-30}^* > 7$, it is considered to be low drag (or hibernation). Here, the superscript $*$ indicates normalization with the instantaneous viscous length scale. It is observed that all the low-drag velocity profiles—both minimal and large domain—show very good agreement. The agreement with lower branch ECS profile is also excellent in the region $y^+ \lesssim 30$.

Finally, we quantify the spatially intermittent nature of hibernation. Figure 21 shows intermittency factors for hibernation based on temporal and spatial sampling techniques: The red line from temporal sampling as one shown in Fig. 10 and the green line is based on spatial sampling and is calculated as

$$F_H = \frac{\sum_{n=1}^{N_H} A_{H,n}}{A}. \quad (7)$$

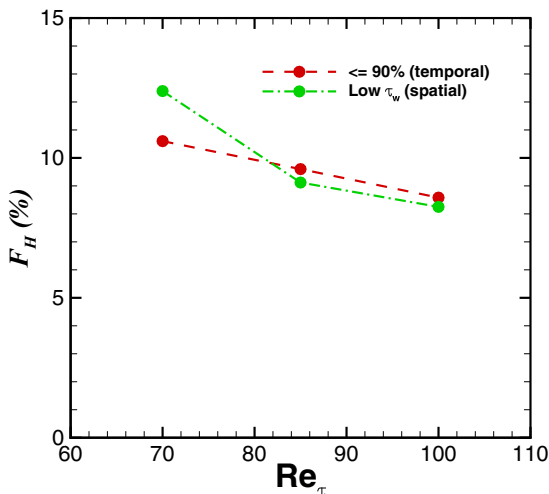


FIG. 21. Intermittency factors for hibernation, both temporal and spatial, as a function of friction Reynolds number.

Here, $A_{H,n}$ is the area of the n th patch of the domain undergoing hibernation at any given time, N_H is the total number of patches in an instantaneous snapshot, and A is the total surface area of the wall. It is observed that first both temporal and spatial intermittency factors are very close to each other for all the Reynolds numbers, and second, as the Reynolds number is increased, the occurrence of hibernation, both temporally and spatially, decreases. It is worth mentioning that, by construction, the spatial separation of hibernation patches is larger than the correlation lengths of the flow. The average separations between the centers of mass of hibernation patches in the streamwise and spanwise directions, respectively, in wall units, are 1131.54×288.14 for $Re_{\tau} = 70$, 1108.87×282.32 for $Re_{\tau} = 85$, and 1113.66×282.19 for $Re_{\tau} = 100$. In other words, they are higher than the correlation lengths in the streamwise and spanwise directions, respectively, by a factor of 1.89×2.88 for $Re_{\tau} = 70$, 1.85×2.82 for $Re_{\tau} = 85$, and 1.86×2.82 for $Re_{\tau} = 100$. There does not seem to be a clear dependence of the mean spatial separation between hibernation patches on Reynolds number, but the area of the region undergoing hibernation does depend on Reynolds number, as already shown in Fig. 21. It is noteworthy that we get nearly identical velocity profiles and intermittency factors from two completely independent thresholding criteria, one based on time and the other based on space.

2. Connections to nonlinear traveling waves

Figure 22 illustrates a bifurcation diagram of average velocity versus friction Reynolds number for the P4 family of minimal domain traveling-wave (TW) solutions discussed in Sec. I. These solutions have streamwise and spanwise periods of length π and $\pi/2$, respectively, in outer units. A solution with higher friction Reynolds number (Re_{τ}) is an upper branch (UB) solution corresponding to high drag, while that with lower Re_{τ} is a lower branch (LB) solution. Curves for the Prandtl–von Kármán and Virk MDR log-law profiles are also shown. In this representation, also known as the Prandtl–von Kármán plot, the lower branch solutions lie above the upper branch solutions, because for the same wall shear stress, a lower branch solution has higher bulk velocity than the upper branch solution. We will make comparisons between extended-domain DNS results and minimal channel ECS at constant mass flux (laminar centerline velocity Re). The DNS at $Re_{\tau} = 70, 85, \text{ and } 100$ have Reynolds numbers based on the laminar centerline velocity (Re) of 1490, 1820, and 2200, respectively. The ECS used for comparison are represented on the plot as red, green, and blue triangles, respectively. Triangles pointing upwards are upper branch solutions whereas triangles pointing downwards are

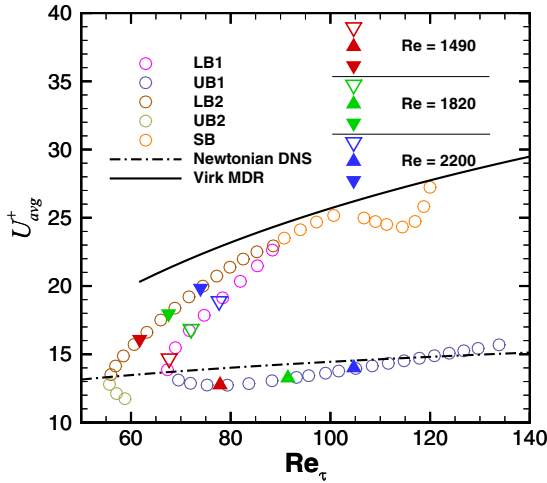


FIG. 22. Prandtl–von Kármán plot of the bifurcation diagram for the P4 family of ECS [28]. The average velocities as a function of friction Reynolds number are shown. Corresponding curves for Newtonian turbulence and Virk MDR are also shown.

lower branch solutions. For the P4 family, there are two lower-branch-solution branches, denoted as LB1 and LB2, and two upper-branch-solution branches, denoted as UB1 and UB2 [28]. Lower branch solutions used for comparison with DNS that lie on the LB1 branch are represented as hollow triangles while the ones that lie on the LB2 branch are represented as filled triangles. Only the solutions that lie on the UB1 upper branch are used for comparison—the UB2 branch has not yet been successfully resolved for higher Re . Mean velocity profiles of these traveling wave solutions are illustrated in Fig. 1(b). A subharmonic branch (SB) arises above the turning point of the LB solutions at $Re_\tau = 88.7$, giving rise to spatiotemporal period doubling—this branch has doubled fundamental spatial periods in the streamwise and spanwise directions compared to the P4 solution family.

It should be kept in mind that the ECS used for comparison here come from one particular family (P4) at one particular domain size. An interesting feature of this family of solutions, as already mentioned earlier, is that the turbulent dynamics in the minimal channel is organized around these ECS. As illustrated in Fig. 1(a), Park and Graham [28] studied connections between traveling wave solutions and turbulent trajectories in a minimal domain, observing that while the dynamical trajectory spends most of the time in one core region of the state space, fluctuating about the upper branch ECS UB1, it occasionally escapes the core region and passes through the vicinity of LB1 solutions, approaching LB2 very closely. In particular, LB2 is the closest approach of the trajectories to the laminar state and seems to form a lower bound of the turbulent trajectory with regard to flow properties like wall shear stress, energy dissipation rate, and turbulent kinetic energy—see Fig. 1(a). This observation is further illustrated in Fig. 23 where we show time series of wall shear stress in minimal channel turbulence at laminar centreline Reynolds numbers of 1490, 1820, and 2200.

To address the relationship between large-box DNS with upper and lower branch ECS, we begin by comparing averages over patches the size of minimal channel ECS in the large domain with the actual ECS. In Fig. 24 we show time series of wall shear stress measured over a patch the size of a minimal channel, $L_x^+ \approx 360, L_z^+ \approx 140$, and compare it with the wall shear stress of the exact coherent states at the same Re .

Due to the saddle-node bifurcation shown in Fig. 22, we observe that the wall shear stress of both LB1 and LB2 decreases as the Reynolds number is increased. The gap between the lower branch ECS and the DNS increases with increasing Reynolds number. The LB2 branch seems to form the lower bound to the wall shear stress for the corresponding large-box DNS; this bound is fairly sharp

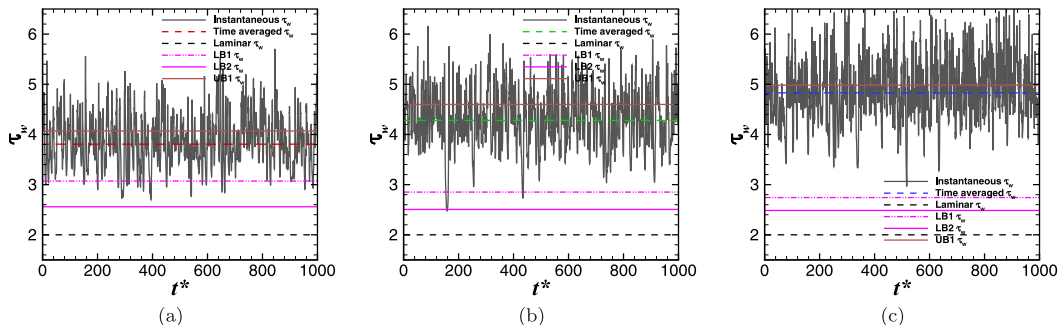


FIG. 23. Time series of the wall shear stress measured in a minimal channel at different Reynolds numbers. Time-averaged values and wall shear stress for upper and lower branch ECS are also shown for comparison. (a) $Re = 1490$, (b) $Re = 1820$, and (c) $Re = 2200$.

at low Re but becomes less so as Re increases. This result is important because the same trend has been observed in minimal channels. In fact, Fig. 24 (minimal patches in the large box) is virtually indistinguishable from Fig. 23 (minimal box). This suggests that localized regions in a large box approach the traveling wave solutions in a way similar to minimal channels.

To make a closer comparison of hibernating turbulence occurring spatially in a large domain with a lower branch ECS, we consider the conditionally averaged velocity field around a point located in the center of an instantaneous patch undergoing hibernation. For DNS at $Re = 1820$, a total number of 26033 low-drag regions or patches are identified using the edge-detection scheme discussed in Sec. III B 1. This amounts to an average of 9 events occurring per field. The conditionally averaged flow field is determined by locating the centroids of all the low-drag patches, shifting the velocity fields such that all centroids coincide, and then averaging them. Reflection symmetry is enforced in the spanwise (neutral) direction. The spatial wall shear stress pattern of the resulting conditionally averaged flow field is shown in Fig. 25. We observe a low-speed streak in the streamwise direction straddled by streamwise vortices. Qualitatively, the picture looks similar to the conditionally averaged wall shear stress patterns obtained by pointwise thresholding [see Fig. 13(b)] except for a couple of differences. First, the spatially sampled streak is not as elongated as the temporally sampled one. Second, the spatially identified streak has a spanwise width a little bit higher than that from temporal sampling.

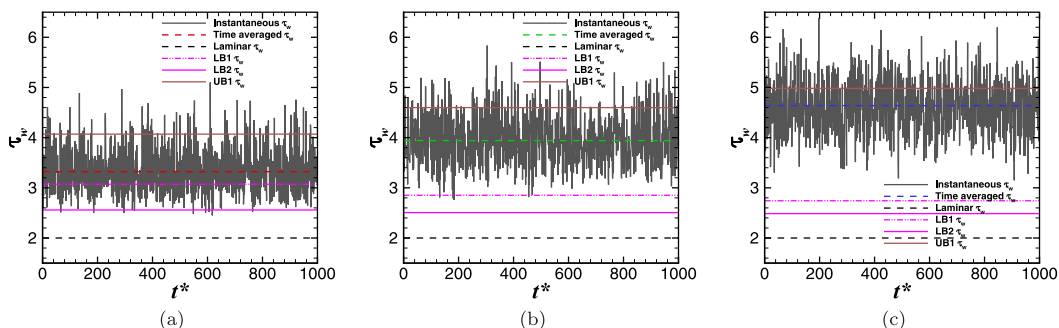


FIG. 24. Time series of the wall shear stress measured over a minimal patch in a large channel at different Reynolds numbers. Time-averaged values and wall shear stress for upper and lower branch ECS are also shown for comparison. (a) $Re = 1490$, (b) $Re = 1820$, and (c) $Re = 2200$.

TEMPORAL AND SPATIAL INTERMITTENCIES WITHIN ...

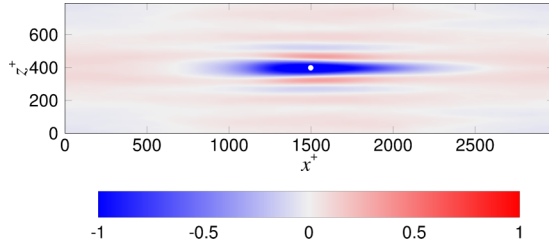


FIG. 25. Spatial patterns of ensemble-averaged wall shear stress fluctuations at $Re_\tau = 85$ ($Re = 1820$). The white dot represents the location at which the centroids of individual low-drag patches were centered.

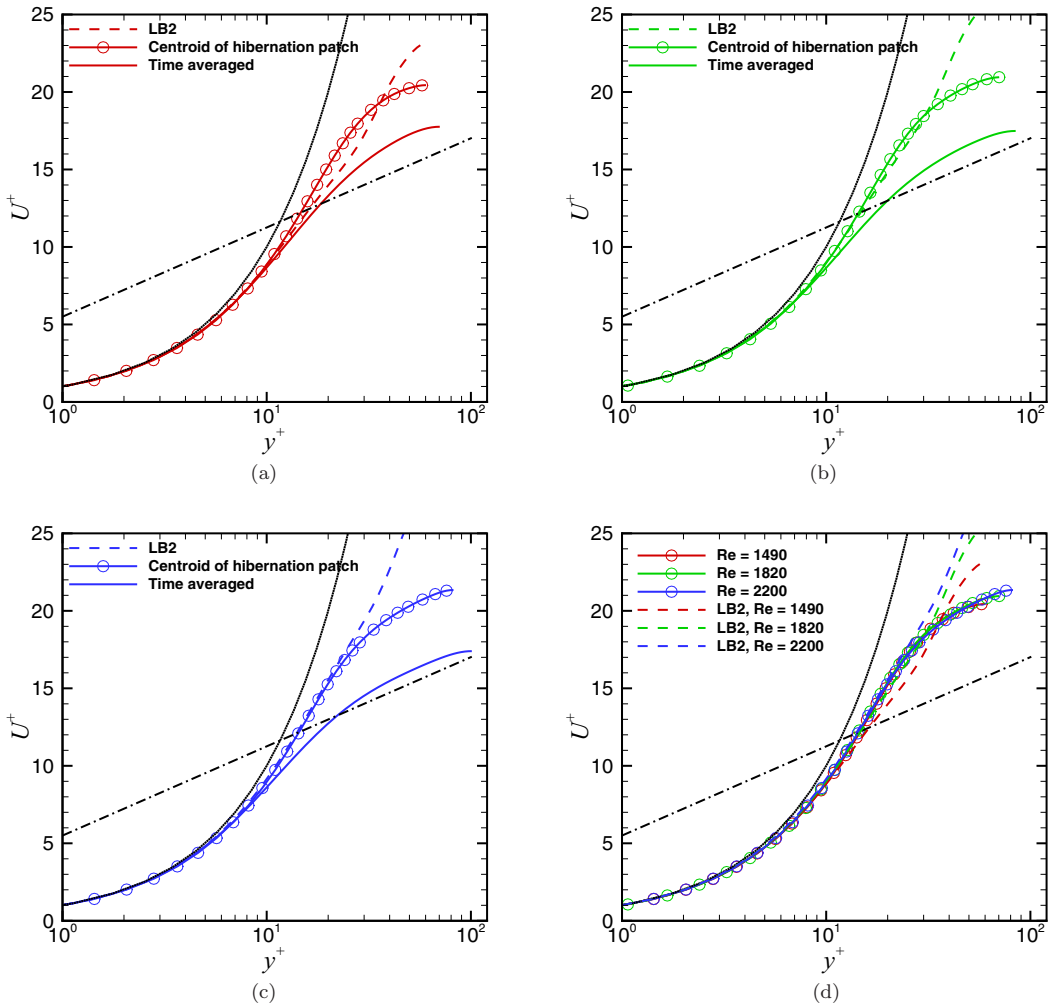


FIG. 26. [(a)–(c)] Comparison of conditional mean velocity profiles at the centroid of hibernation patches in a large box with lower branch ECS at the same Reynolds number. (d) All the conditionally averaged velocity profiles at the centroids of hibernation patches at different Reynolds numbers. (a) $Re = 1490$, (b) $Re = 1820$, (c) $Re = 2200$, and (d) all Re values.

Illustrated in Fig. 26 are conditionally averaged mean velocity profiles at the centroid of hibernation regions occurring spatially. For example, the hibernation profile in Fig. 26(b) corresponds to the streamwise velocity profile observed at the white dot in Fig. 25. As we have done everywhere, each velocity profile plotted in Fig. 26 is scaled with the corresponding mean wall shear stress, unconditional or conditional as the case may be. This is why they all collapse in the near-wall region. For all the three cases, we observe that the velocity profiles at the centroid of hibernation patches are elevated: They lie well above the unconditional time averaged profiles from DNS and very close to the lower branch ECS. In fact, in the region $y^+ \lesssim 30$, both the conditional and ECS velocity profiles are very similar, and become nearly indistinguishable as the Reynolds number is increased. However, the behavior in the core (near the centreline) remains distinct. Similar observations were made while comparing lower branch ECS profiles with conditionally averaged (low-drag) profiles from temporal and spatial sampling techniques [Figs. 11(a) and 19]. This pattern is also observed by other researchers when comparing ECS to minimal channel turbulence [28,91] and localized relative

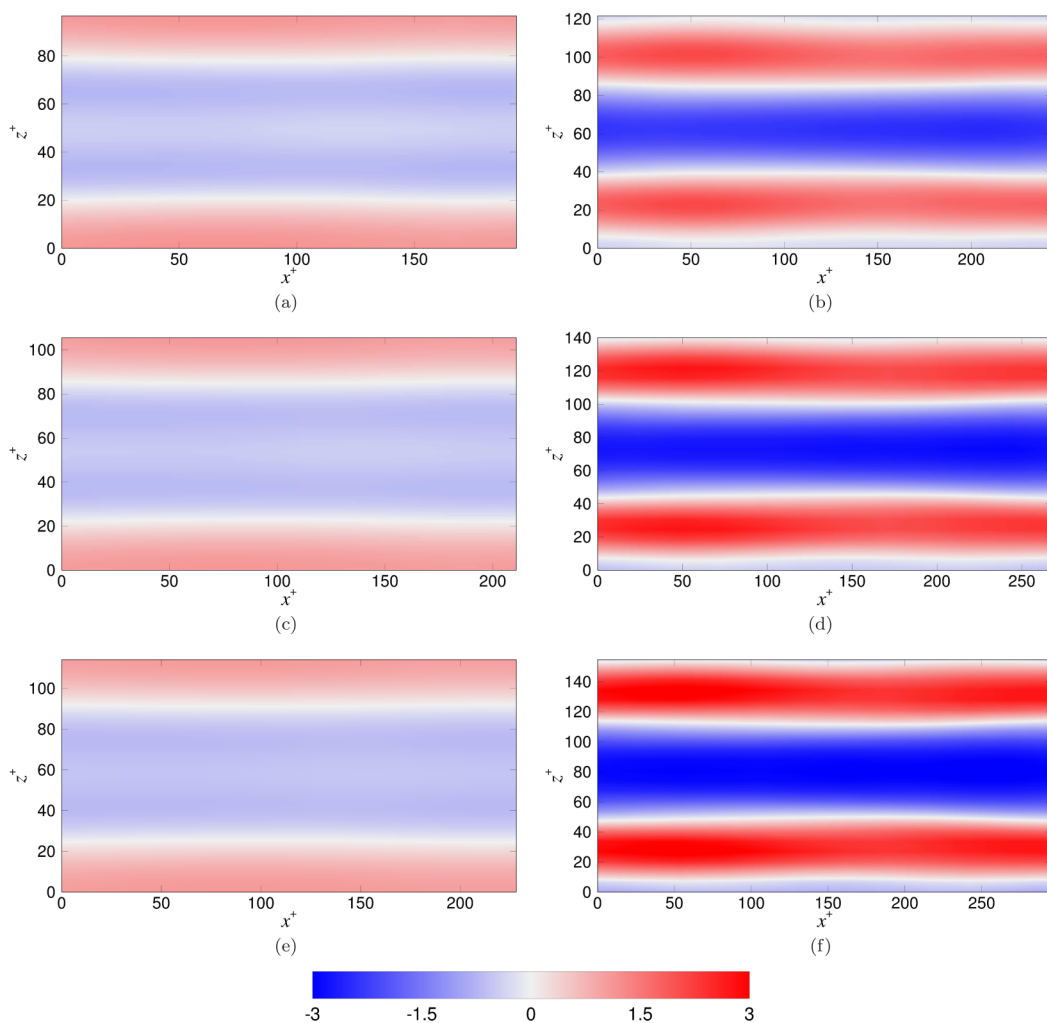


FIG. 27. Spatial patterns of wall shear stress fluctuations of P4 lower and upper branch traveling wave solutions. (a) $Re = 1490$, LB2, (b) $Re = 1490$, UB1, (c) $Re = 1820$, LB2, (d) $Re = 1820$, UB1, (e) $Re = 2200$, LB2, and (f) $Re = 2200$, UB1.

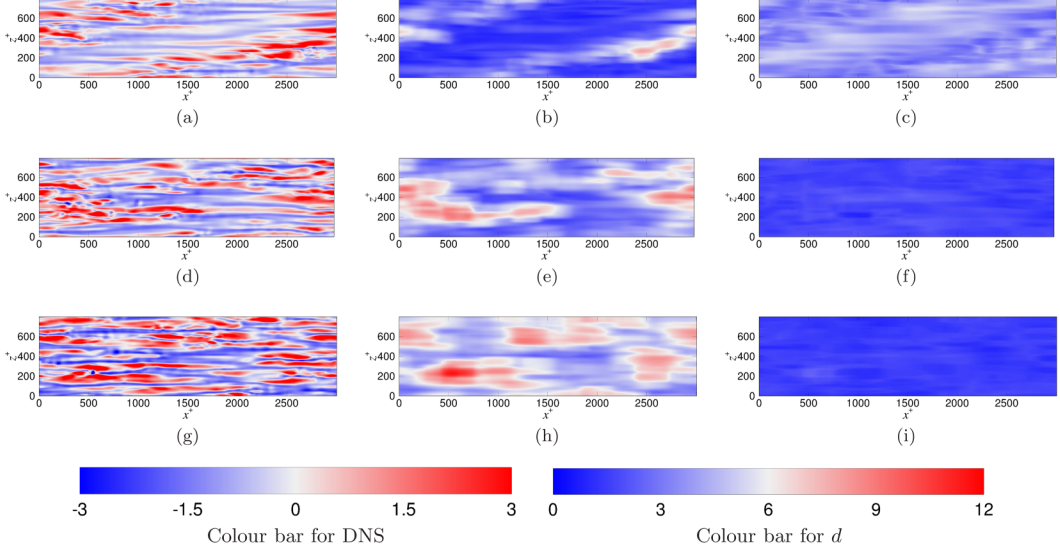


FIG. 28. [(a), (d), (g)] Spatial patterns of instantaneous wall shear stress fluctuations from DNS. [(b), (e), (h)] Distance between DNS and lower branch ECS that lie on LB2. [(c), (f), (i)] Distance between DNS and upper branch ECS that lie on UB1. (a) $\text{Re} = 1490$, DNS, (b) $\text{Re} = 1490$, d_{LB2} , (c) $\text{Re} = 1490$, d_{UB1} , (d) $\text{Re} = 1820$, DNS, (e) $\text{Re} = 1820$, d_{LB2} , (f) $\text{Re} = 1820$, d_{UB1} , (g) $\text{Re} = 2200$, DNS, (h) $\text{Re} = 2200$, d_{LB2} , and (i) $\text{Re} = 2200$, d_{UB1} .

periodic orbits (RPOs) / lower branch solution to turbulent puffs in pipe flows [32]—it seems that a single ECS is not capable of capturing both near-wall and core dynamics. The close similarity for $y^+ \lesssim 30$ again suggests that a hibernation event in an extended domain is, at least with regard to mean velocity, a spatially local approach toward a lower branch ECS. In Fig. 26(d), conditional streamwise velocity profiles observed at the centroid of hibernation regions are presented as a function of Reynolds number. There does not seem to exist an obvious dependence on Reynolds number.

We now propose a way of quantifying the local closeness of a DNS to lower and upper branch exact coherent states. We consider instantaneous snapshots of spatial patterns of wall shear stress. See Fig. 5 for some examples of snapshots at $\text{Re}_\tau = 70, 85$, and 100; here we will be using the snapshots from the right column to make comparisons with the traveling wave solutions [plotted again in Figs. 28(a), 28(d), and 28(g)]. We calculate how closely a localized coherent structure from a DNS snapshot resembles the chosen ECS based on the wall shear stress measurements. In particular, we calculate the following function:

$$d(x, z, t) = \min_{\phi} \left(\frac{1}{L'_x L'_z} \sqrt{\int_{x-\frac{L'_x}{2}}^{x+\frac{L'_x}{2}} \int_{z-\frac{L'_z}{2}}^{z+\frac{L'_z}{2}} \{f(x', z', t) - g(x', z', t, \phi)\}^2 dx' dz'} \right) \quad (8)$$

Here, d is the “distance” between DNS and ECS, f is a flow property from the DNS and g is the same flow property from the traveling wave or a reference template, x and z are the coordinates in space, ϕ represents the spatial phases in x and z of g relative to f , and $L'_x = \pi$ and $L'_z = \pi/2$ are the streamwise and spanwise periods, respectively, of the ECS we are using for comparison. Since we have chosen to quantify the closeness based on wall shear stresses, here $f = \tau_{w, \text{DNS}}(x, z, t)$ and $g = \tau_{w, \text{TW}}(x, z)$. Shown in Fig. 27 are wall shear stress fluctuation patterns of the lower (LB2) and upper (UB1) branch traveling wave solutions of the P4 family used as templates for comparison with

DNS. Figures 28(b), 28(e), and 28(h) show instantaneous spatial variation of d when the reference template is wall shear stress of a lower branch traveling wave. It can be observed that bluer regions that have smaller values of d are the ones that are much closer to the lower branch traveling wave and thus exhibit low drag. On the other hand, regions that are more red are characteristic of high drag. In Figs. 28(c), 28(f), and 28(i), the distance of DNS from the upper branch traveling wave is shown. A red region in this figure may not necessarily mean low drag, but could also mean a high-drag region due to hyperactive or active (normal) turbulence that is just different from the upper branch traveling wave used here for comparison. On the other hand, a blue region on this figure would mean that it is close to the upper branch and will exhibit high drag.

To summarize, a number of separate results, from time series of wall shear stress to conditional mean velocity profiles to a measure of local similarity between wall shear stress patterns suggest that near-wall features of exact coherent states found in minimal channels appear in a spatiotemporally local manner in extended domains. In summary, the results presented here suggest that spatiotemporal intermittency in transitional channel flow turbulence is related to temporal intermittency, and by extension to the state space structure, in the minimal channel.

IV. CONCLUSIONS

The present work has quantified, using temporal and spatial sampling and conditional averaging techniques, the intermittent dynamics of transitional channel flow turbulence in an extended domain. In minimal domains, turbulence in this Reynolds number range displays substantial intermittency that is associated with chaotic movement of turbulent trajectories between lower and upper branch invariant solutions known as exact coherent states (ECS). In the present work we address the relationship between temporal dynamics in minimal channels and spatiotemporal dynamics in extended domains. Both temporal and spatial analyses of the turbulent velocity fields are performed, the latter using image analysis methods. These analyses partition the flow characteristics into three classes depending on degree of turbulence activity; we present the differences between flows fields in these classes in terms of simple quantities such as mean velocity, wall shear stress, and flow structures. Notably, the temporal and spatial analysis methods, although completely independent of one another, yield very similar results for both low- and high-drag regions. The conditional mean velocity profiles during low-drag events in large domains, both temporal and spatial, closely resemble those found in low-drag temporal intervals in the minimal channel. Finally, we present connections between turbulence and exact coherent states by comparing wall shear stress in localized patches the size of minimal channels in large domains with those in actual minimal channel. Conditional mean velocity profiles during low-drag intervals occurring temporally and spatially in extended domains were compared with the lower branch ECS profiles from the P4 family of solutions and an excellent agreement was found in the region $y^+ \lesssim 30$. This analysis shows that, at least with regard to the quantities studied here, the near-wall flow structure in the low-drag patches of the large domain resembles that of a lower branch ECS. A clear direction for future work is development of methods to extend the comparison to incorporate more details of the velocity fields.

We believe that these results have the potential to shed light on the structure and dynamics of laminar intervals in the laminar-turbulent transition regime, especially as Reynolds number increases toward the uniformly turbulent regime. In particular, our work is consistent with that of Avila *et al.* [77], who note that intermittent low-drag excursions persist into the fully turbulent regime. We find that although low-drag hibernating events become increasingly rare as Re increases, their structure, especially in terms of conditional mean velocity profile, is insensitive to Re. Finally, the results presented here suggest that spatiotemporal intermittency in transitional channel flow turbulence is related to temporal intermittency, and by extension to the state space structure, in the minimal channel. The similarity in near wall structure, especially wall shear stress and conditional mean velocity profile, suggests that ECS found in a minimal channel continue to play some role in organizing the spatiotemporal dynamics in extended domains.

ACKNOWLEDGMENTS

This work has been supported by the National Science Foundation through Grants No. CBET-1066223 and No. CBET-1510291 (Fluid Dynamics Program), and the Air Force Office of Scientific Research through Grants No. FA9550-11-1-0094 and No. FA9550-15-1-0062 (Flow Interactions and Control Program). The DNS code used here, ChannelFlow [81], was developed and distributed by John F Gibson at the University of New Hampshire.

-
- [1] B. Hof, C. W. H. van Doorne, J. Westerweel, F. T. M. Nieuwstadt, H. Faisst, B. Eckhardt, H. Wedin, R. R. Kerswell, and F. Waleffe, Experimental observation of nonlinear traveling waves in turbulent pipe flow, *Science* **305**, 1594 (2004).
 - [2] R. R. Kerswell, Recent progress in understanding the transition to turbulence in a pipe, *Nonlinearity* **18**, R17 (2005).
 - [3] B. Eckhardt, T. M. Schneider, B. Hof, and J. Westerweel, Turbulence transition in pipe flow, *Annu. Rev. Fluid Mech.* **39**, 447 (2007).
 - [4] A. P. Willis, J. Peixinho, R. R. Kerswell, and T. Mullin, Experimental and theoretical progress in pipe flow transition, *Philos. Trans. R. Soc., A* **366**, 2671 (2008).
 - [5] G. Kawahara, M. Uhlmann, and L. van Veen, The significance of simple invariant solutions in turbulent flows, *Annu. Rev. Fluid Mech.* **44**, 203 (2012).
 - [6] M. Nagata, Three-dimensional finite-amplitude solutions in plane Couette flow: Bifurcation from infinity, *J. Fluid Mech.* **217**, 519 (1990).
 - [7] R. M. Clever and F. H. Busse, Tertiary and quaternary solutions for plane Couette flow, *J. Fluid Mech.* **344**, 137 (1997).
 - [8] M. Nagata, Three-dimensional traveling-wave solutions in plane Couette flow, *Phys. Rev. E* **55**, 2023 (1997).
 - [9] D. Viswanath, Recurrent motions within plane Couette turbulence, *J. Fluid Mech.* **580**, 339 (2007).
 - [10] J. F. Gibson, J. Halcrow, and P. Cvitanović, Visualizing the geometry of state space in plane Couette flow, *J. Fluid Mech.* **611**, 107 (2008).
 - [11] J. F. Gibson, J. Halcrow, and P. Cvitanović, Equilibrium and travelling-wave solutions of plane Couette flow, *J. Fluid Mech.* **638**, 243 (2009).
 - [12] J. Halcrow, J. F. Gibson, P. Cvitanović, and D. Viswanath, Heteroclinic connections in plane Couette flow, *J. Fluid Mech.* **621**, 365 (2009).
 - [13] T. Itano and S. C. Generalis, Hairpin Vortex Solution in Planar Couette Flow: A Tapestry of Knotted Vortices, *Phys. Rev. Lett.* **102**, 114501 (2009).
 - [14] T. M. Schneider, J. F. Gibson, and J. Burke, Snakes and Ladders: Localized Solutions of Plane Couette Flow, *Phys. Rev. Lett.* **104**, 104501 (2010).
 - [15] K. Deguchi, P. Hall, and A. Walton, The emergence of localized vortex-wave interaction states in plane Couette flow, *J. Fluid Mech.* **721**, 58 (2013).
 - [16] H. M. Blackburn, P. Hall, and S. J. Sherwin, Lower branch equilibria in Couette flow: The emergence of canonical states for arbitrary shear flows, *J. Fluid Mech.* **726**, R2 (2013).
 - [17] M. Nagata, A note on the mirror-symmetric coherent structure in plane Couette flow, *J. Fluid Mech.* **727**, R1 (2013).
 - [18] F. Waleffe, Three-Dimensional Coherent States in Plane Shear Flows, *Phys. Rev. Lett.* **81**, 4140 (1998).
 - [19] F. Waleffe, Exact coherent structures in channel flow, *J. Fluid Mech.* **435**, 93 (2001).
 - [20] F. Waleffe, Homotopy of exact coherent structures in plane shear flows, *Phys. Fluids* **15**, 1517 (2003).
 - [21] S. Toh and T. Itano, A periodic-like solution in channel flow, *J. Fluid Mech.* **481**, 67 (2003).
 - [22] M. Nagata and K. Deguchi, Mirror-symmetric exact coherent states in plane Poiseuille flow, *J. Fluid Mech.* **735**, R4 (2013).
 - [23] H. Faisst and B. Eckhardt, Traveling Waves in Pipe Flow, *Phys. Rev. Lett.* **91**, 224502 (2003).

- [24] H. Wedin and R. R. Kerswell, Exact coherent structures in pipe flow: Travelling wave solutions, *J. Fluid Mech.* **508**, 333 (2004).
- [25] R. R. Kerswell and O. R. Tutty, Recurrence of travelling waves in transitional pipe flow, *J. Fluid Mech.* **584**, 69 (2007).
- [26] C. C. T. Pringle and R. R. Kerswell, Asymmetric, Helical, and Mirror-Symmetric Traveling Waves in Pipe Flow, *Phys. Rev. Lett.* **99**, 074502 (2007).
- [27] Y. Duguet, C. C. T. Pringle, and R. R. Kerswell, Relative periodic orbits in transitional pipe flow, *Phys. Fluids* **20**, 114102 (2008).
- [28] J. S. Park and M. D. Graham, Exact coherent states and connections to turbulent dynamics in minimal channel flow, *J. Fluid Mech.* **782**, 430 (2015).
- [29] E. Brand and J. F. Gibson, A doubly localized equilibrium solution of plane Couette flow, *J. Fluid Mech.* **750**, R3 (2014).
- [30] M. Chantry, A. P. Willis, and R. R. Kerswell, Genesis of Streamwise-Localized Solutions from Globally Periodic Traveling Waves in Pipe Flow, *Phys. Rev. Lett.* **112**, 164501 (2014).
- [31] S. Zammert and B. Eckhardt, Streamwise and doubly-localised periodic orbits in plane Poiseuille flow, *J. Fluid Mech.* **761**, 348 (2014).
- [32] M. Avila, F. Mellibovsky, N. Roland, and B. Hof, Streamwise-Localized Solutions at the Onset of Turbulence in Pipe Flow, *Phys. Rev. Lett.* **110**, 224502 (2013).
- [33] T. Itano and S. Toh, The dynamics of bursting process in wall turbulence, *J. Phys. Soc. Jpn.* **70**, 703 (2001).
- [34] S. Rawat, C. Cossu, and F. Rincon, Travelling-wave solutions bifurcating from relative periodic orbits in plane Poiseuille flow, *C. R. Mec.* **344**, 448 (2016).
- [35] P. S. Virk, Drag reduction fundamentals, *AIChE J.* **21**, 625 (1975).
- [36] R. R. Kerswell, D. Obrist, and P. J. Schmid, On smoothed turbulent shear flows: Bounds, numerics, and stress-reducing additives, *Phys. Fluids* **15**, 78 (2003).
- [37] P. R. Bandyopadhyay, Stokes mechanism of drag reduction, *J. Appl. Mech.* **73**, 483 (2006).
- [38] L. Xi and M. D. Graham, Turbulent drag reduction and multistage transitions in viscoelastic minimal flow units, *J. Fluid Mech.* **647**, 421 (2010).
- [39] L. Xi and M. D. Graham, Active and Hibernating Turbulence in Minimal Channel Flow of Newtonian and Polymeric Fluids, *Phys. Rev. Lett.* **104**, 218301 (2010).
- [40] Y. Dubief, C. M. White, E. S. G. Shaqfeh, and V. E. Terrapon, Polymer maximum drag reduction: A unique transitional state, *Cent. Turbul. Res. Annu. Res. Briefs*, 47 (2010).
- [41] L. Xi and M. D. Graham, Dynamics on the Laminar-Turbulent Boundary and the Origin of the Maximum Drag Reduction Asymptote, *Phys. Rev. Lett.* **108**, 028301 (2012).
- [42] L. Xi and M. D. Graham, Intermittent dynamics of turbulence hibernation in Newtonian and viscoelastic minimal channel flows, *J. Fluid Mech.* **693**, 433 (2012).
- [43] J. Jiménez and P. Moin, The minimal flow unit in near-wall turbulence, *J. Fluid Mech.* **225**, 213 (1991).
- [44] P. Manneville, On the transition to turbulence of wall-bounded flows in general, and plane Couette flow in particular, *Eur. J. Mech. B* **49**, 345 (2015).
- [45] I. J. Wygnanski and F. H. Champagne, On transition in a pipe, part 1. The origin of puffs and slugs and the flow in a turbulent slug, *J. Fluid Mech.* **59**, 281 (1973).
- [46] I. Wygnanski, M. Sokolov, and D. Friedman, On transition in a pipe, part 2. The equilibrium puff, *J. Fluid Mech.* **69**, 283 (1975).
- [47] K. Avila, D. Moxey, A. de Lozar, M. Avila, D. Barkley, and B. Hof, The onset of turbulence in pipe flow, *Science* **333**, 192 (2011).
- [48] D. Barkley, Simplifying the complexity of pipe flow, *Phys. Rev. E* **84**, 016309 (2011).
- [49] D. Barkley, B. Song, V. Mukund, G. Lemoult, M. Avila, and B. Hof, The rise of fully turbulent flow, *Nature (London)* **526**, 550 (2015).
- [50] M. D. Graham, Fluid dynamics: Turbulence spreads like wildfire, *Nature (London)* **526**, 508 (2015).
- [51] M. Avila and B. Hof, Nature of laminar-turbulence intermittency in shear flows, *Phys. Rev. E* **87**, 063012 (2013).
- [52] I. Wygnanski, M. Sokolov, and D. Friedman, On a turbulent “spot” in a laminar boundary layer, *J. Fluid Mech.* **78**, 785 (1976).

- [53] H. W. Emmons, The laminar-turbulent transition in a boundary layer, part I, *J. Aeronaut. Sci.* **18**, 490 (1951).
- [54] K. P. Nolan and T. A. Zaki, Conditional sampling of transitional boundary layers in pressure gradients, *J. Fluid Mech.* **728**, 306 (2013).
- [55] D. R. Carlson, S. E. Widnall, and M. F. Peeters, A flow-visualization study of transition in plane Poiseuille flow, *J. Fluid Mech.* **121**, 487 (1982).
- [56] Y. Duguet and P. Schlatter, Oblique Laminar-Turbulent Interfaces in Plane Shear Flows, *Phys. Rev. Lett.* **110**, 034502 (2013).
- [57] G. Lemoult, J.-L. Aider, and J. E. Wesfreid, Experimental scaling law for the subcritical transition to turbulence in plane Poiseuille flow, *Phys. Rev. E* **85**, 025303 (2012).
- [58] G. Lemoult, J.-L. Aider, and J. E. Wesfreid, Turbulent spots in a channel: Large-scale flow and self-sustainability, *J. Fluid Mech.* **731**, R1 (2013).
- [59] G. Lemoult, K. Gumowski, J.-L. Aider, and J. E. Wesfreid, Turbulent spots in channel flow: An experimental study, *Eur. Phys. J. E* **37**, 25 (2014).
- [60] S. Hashimoto, A. Hasobe, T. Tsukahara, Y. Kawaguchi, and H. Kawamura, An experimental study on turbulent-stripe structure in transitional channel flow, in *Proceedings of the Sixth International Symposium On Turbulence, Heat and Mass Transfer - Rome, Italy* (Begell House, 2009), p. 193.
- [61] J. Rolland, Stochastic analysis of the time evolution of laminar-turbulent bands of plane Couette flow, *Eur. Phys. J. E* **38**, 121 (2015).
- [62] L. S. Tuckerman, T. Kreilos, H. Schrobdsdorff, T. M. Schneider, and J. F. Gibson, Turbulent-laminar patterns in plane Poiseuille flow, *Phys. Fluids* **26**, 114103 (2014).
- [63] D. Barkley and L. S. Tuckerman, Computational Study of Turbulent Laminar Patterns in Couette Flow, *Phys. Rev. Lett.* **94**, 014502 (2005).
- [64] R. J. Volino, M. P. Schultz, and C. M. Pratt, Conditional sampling in a transitional boundary layer under high freestream turbulence conditions, *J. Fluids Eng.* **125**, 28 (2003).
- [65] N. Hutchins, J. P. Monty, B. Ganapathisubramani, H. C. H. Ng, and I. Marusic, Three-dimensional conditional structure of a high-Reynolds-number turbulent boundary layer, *J. Fluid Mech.* **673**, 255 (2011).
- [66] N. Hutchins and I. Marusic, Large-scale influences in near-wall turbulence, *Philos. Trans. R. Soc., A* **365**, 647 (2007).
- [67] J. C. del Álamo, J. Jiménez, P. Zandonade, and R. D. Moser, Self-similar vortex clusters in the turbulent logarithmic region, *J. Fluid Mech.* **561**, 329 (2006).
- [68] E. Kaiser, B. R. Noack, L. Cordier, A. Spohn, M. Segond, M. Abel, G. Daviller, J. Östh, S. Krajnović, and R. K. Niven, Cluster-based reduced-order modelling of a mixing layer, *J. Fluid Mech.* **754**, 365 (2014).
- [69] N. Otsu, A threshold selection method from gray-level histograms, *IEEE Trans. Syst. Man. Cybern.* **9**, 62 (1979).
- [70] D. Liu and J. Yu, Otsu method and K-means, in *Proceedings of the Ninth International Conference on Hybrid Intelligent Systems - Shenyang, China*, Vol. 1 (IEEE, 2009), p. 344.
- [71] B. Rehill, E. J. Walsh, L. Brandt, P. Schlatter, T. A. Zaki, and D. M. McEligot, Identifying turbulent spots in transitional boundary layers, *J. Turbomach.* **135**, 011019 (2012).
- [72] J. R. Baltzer, R. J. Adrian, and X. Wu, Structural organization of large and very large scales in turbulent pipe flow simulation, *J. Fluid Mech.* **720**, 236 (2013).
- [73] D. J. C. Dennis and T. B. Nickels, Experimental measurement of large-scale three-dimensional structures in a turbulent boundary layer, part 2. Long structures, *J. Fluid Mech.* **673**, 218 (2011).
- [74] J. H. Lee and H. J. Sung, Very-large-scale motions in a turbulent boundary layer, *J. Fluid Mech.* **673**, 80 (2011).
- [75] J. Lee, J. H. Lee, J.-I. Choi, and H. J. Sung, Spatial organization of large- and very-large-scale motions in a turbulent channel flow, *J. Fluid Mech.* **749**, 818 (2014).
- [76] J. Lee, J. Ahn, and H. J. Sung, Comparison of large- and very-large-scale motions in turbulent pipe and channel flows, *Phys. Fluids* **27**, 025101 (2015).
- [77] M. Avila, A. P. Willis, and B. Hof, On the transient nature of localized pipe flow turbulence, *J. Fluid Mech.* **646**, 127 (2010).

- [78] J. Jiménez, G. Kawahara, M. P. Simens, M. Nagata, and M. Shiba, Characterization of near-wall turbulence in terms of equilibrium and “bursting” solutions, *Phys. Fluids* **17**, 015105 (2005).
- [79] O. Flores and J. Jiménez, Hierarchy of minimal flow units in the logarithmic layer, *Phys. Fluids* **22**, 071704 (2010).
- [80] J. Jiménez, Near-wall turbulence, *Phys. Fluids* **25**, 101302 (2013).
- [81] J. F. Gibson, Channelflow: A spectral Navier-Stokes simulator in C++, Tech. Rep., University of New Hampshire, 2009.
- [82] R. Peyret, *Spectral Methods for Incompressible Viscous Flow* (Springer-Verlag, New York, 2002).
- [83] G. Alfonsi, On direct numerical simulation of turbulent flows, *Appl. Mech. Rev.* **64**, 020802 (2011).
- [84] G. A. Webber, R. A. Handler, and L. Sirovich, The Karhunen-Loève decomposition of minimal channel flow, *Phys. Fluids* **9**, 1054 (1997).
- [85] V. C. Patel and M. R. Head, Some observations on skin friction and velocity profiles in fully developed pipe and channel flows, *J. Fluid Mech.* **38**, 181 (1969).
- [86] N. Kasagi and N. Shikazono, Contribution of direct numerical simulation to understanding and modelling turbulent transport, *Proc. Math. Phys. Sci.* **451**, 257 (1995).
- [87] T. Tsukahara, Y. Seki, H. Kawamura, and D. Tochio, DNS of turbulent channel flow at very low Reynolds numbers, in *Proceedings of the Fourth International Symposium on Turbulence and Shear Flow Phenomena TSFP-4 - Williamsburg, VA* (Begell House, 2005), p. 935.
- [88] P. S. Virk, H. S. Mickley, and K. A. Smith, The ultimate asymptote and mean flow structure in Toms’ phenomenon, *J. Appl. Mech.* **37**, 488 (1970).
- [89] M. D. Graham, Drag reduction and the dynamics of turbulence in simple and complex fluids, *Phys. Fluids* **26**, 101301 (2014).
- [90] A. V. Johansson, P. H. Alfredsson, and J. Kim, Evolution and dynamics of shear-layer structures in near-wall turbulence, *J. Fluid Mech.* **224**, 579 (1991).
- [91] Y. Hwang, A. P. Willis, and C. Cossu, Invariant solutions of minimal large-scale structures in turbulent channel flow for Re_τ up to 1000, *J. Fluid Mech.* **802**, R1 (2016).